Crustal growth during back-arc closure: Cretaceous exhumation history of Cordillera Darwin, southern Patagonia

K. T. MALONEY,[1] G. L. CLARKE,[1] K. A. KLEPEIS,[2] C. M. FANNING[3] AND W. WANG[1]
[1]*School of Geosciences, University of Sydney, Sydney, NSW 2006, Australia (kayla.maloney@sydney.edu.au)*
[2]*Department of Geology, University of Vermont, Burlington, VT, USA*
[3]*Research School of Earth Sciences, Australian National University, Canberra, ACT, Australia*

ABSTRACT
The Cordillera Darwin metamorphic complex is unique in the Andes in exposing kyanite–staurolite schist north of the Beagle Channel in southern Patagonia. Garnet in amphibolite facies pelitic schists from Bahía Pia has patchy textures whereby some grains consist of clear, grossular-rich garnet with fine-grained S1 inclusion trails truncated by regions of turbid spessartine–pyrope-rich garnet with biotite, muscovite, plagioclase and quartz inclusions. Micron-scale aqueous inclusions in turbid garnet are consistent with recrystallization facilitated by fluid ingress; S2 inclusion trails indicate this was broadly contemporary with the growth of kyanite and staurolite in the matrix. Pseudosection modelling in Na$_2$O–CaO–K$_2$O–FeO–MgO–Al$_2$O$_3$–SiO$_2$–H$_2$O–TiO$_2$–Fe$_2$O$_3$ (NCKFMASHTO) is used to infer a *P–T* path dominated by decompression from 12 to 9 kbar at $T \approx 620\,°C$, coupled with garnet mode decreasing from ~5% to <1%. U–Th–Pb *in situ* dating of S2 monazite indicates that staurolite and kyanite growth and thus exhumation was underway before 72.6 ± 1.1 Ma. Contact aureoles developed adjacent to late granite intrusions include sillimanite-bearing migmatites formed at $P \approx 6$ kbar after 72 Ma. Metamorphism of southern Cordillera Darwin induced by continental underthrusting beneath the arc, related to closure of the Rocas Verdes back-arc basin, was terminated by thrusting-controlled exhumation, with the rocks at $P \approx 9$ kbar by *c.* 73 Ma and 6 kbar by *c.* 70 Ma.

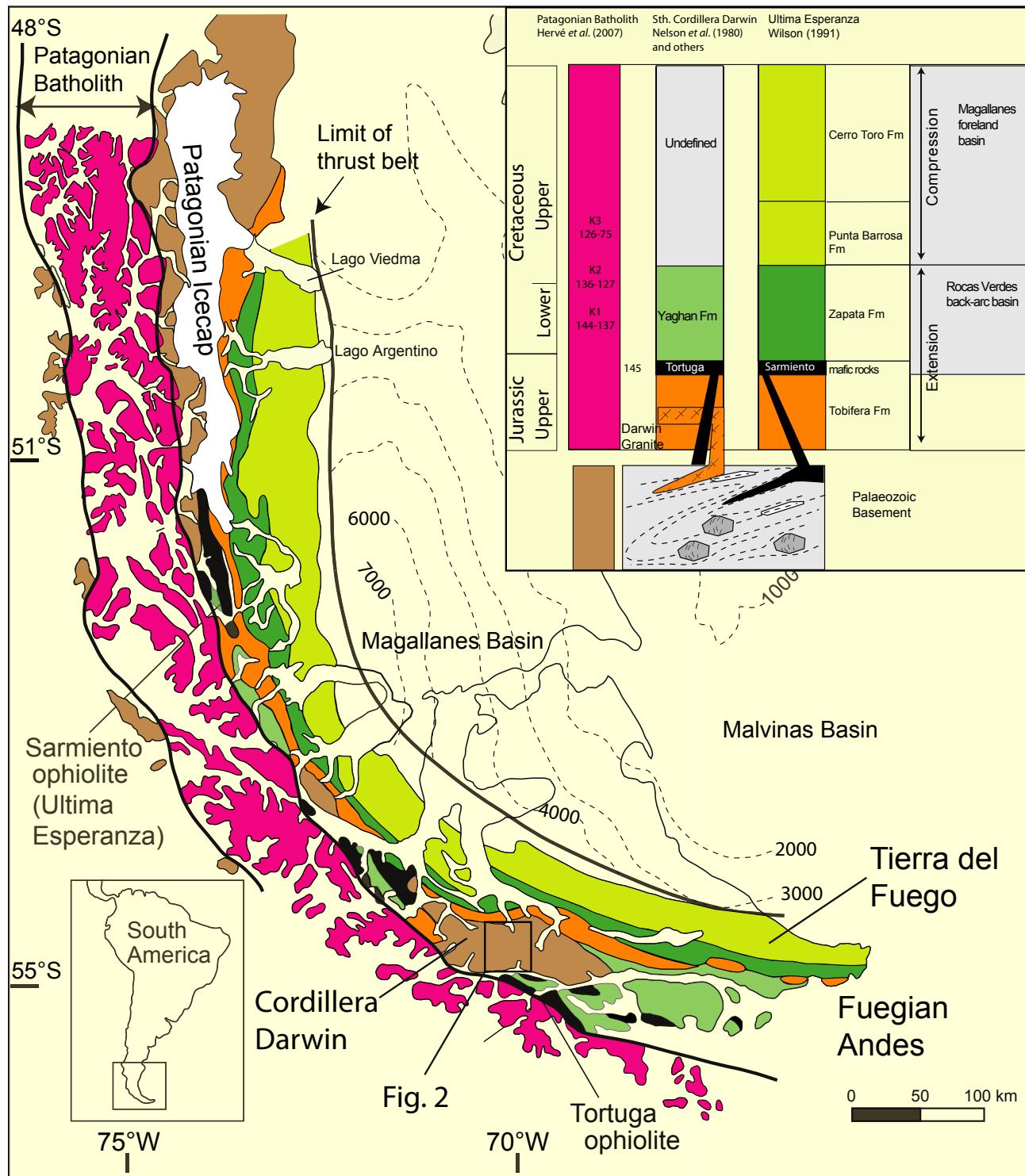**Key words:** Cordillera Darwin; *in situ* monazite; pseudosection; THERMOCALC.

INTRODUCTION

Cordillera Darwin, in southernmost South America (Fig. 1), forms a topographic high that lies, on average, more than 1 km above the surrounding mountains in the Fuegian Andes (Kranck, 1932; Nelson *et al.*, 1980; Klepeis, 1994a; Cunningham, 1995; Kohn *et al.*, 1995). It includes a basement of Palaeozoic schists (Hervé *et al.*, 2010) surrounded by mid-Jurassic and younger volcano-sedimentary cover, and intruded by granite suites and mafic dykes (Fig. 2). North of the Beagle Channel, upper amphibolite facies regional metamorphic assemblages (Darwin, 1846; Nelson *et al.*, 1980; Halpern, 1973; Kohn *et al.*, 1993) occur in basement and cover rocks exposed in a partially ice-covered mountain range between Bahías Pia and Parry (Fig. 2). This belt of high-grade rocks is restricted to a south-east-trending lens (50 × 30 km) that includes exposures at Bahía Pia, Ventisquero Roncagli and Bahía Parry (Dalziel & Cortés, 1972; Nelson *et al.*, 1980; Hervé *et al.*, 1981; Klepeis *et al.*, 2010).

Low-grade remnants of the mid-Jurassic to Early Cretaceous Rocas Verdes back-arc basin occur south of the Beagle Channel (Katz, 1973; Dalziel *et al.*, 1974;

Nelson *et al.*, 1980; Cunningham, 1994). This rift basin is unusual in the Andes because it is the only one of several mid to Late Jurassic basins south of Ecuador that was floored by basaltic crust with mid-ocean ridge affinities (Stern, 1980; Allen, 1982; Alabaster & Storey, 1990; Mpodozis & Allmendinger, 1993; Calderón *et al.*, 2007). Part of the oceanic floor and sedimentary fill of the Rocas Verdes basin occurs tectonically interleaved with basement rocks in Cordillera Darwin (Klepeis *et al.*, 2010). However, heterogeneous effects of Cretaceous deformation and metamorphism make distinguishing the protoliths of units in high-grade components of Cordillera Darwin difficult (Nelson *et al.*, 1980; Hervé *et al.*, 2010).

This paper addresses two major problems: crustal growth mechanisms in a back-arc setting and the metamorphic history of mineral assemblages unique along the Andean chain. We use new data to evaluate conflicting models proposed to explain the occurrence of the Cretaceous regional metamorphic rocks, and propose a tectonic model that accounts for the succession of mineral assemblages in the context of field relationships. These data include the first monazite ages that precisely establish that regional metamorphism occurred during the Late Cretaceous, field

Fig. 1. Simplified geology and stratigraphy of the southern Andes, after Dalziel (1981) and Wilson (1991). Magallanes Basin structure contours demarcate depth to top of Jurassic volcanic rocks, in metres (from Biddle *et al.*, 1986). In the stratigraphic column, K1, K2 and K3 indicate Cretaceous stages of pluton emplacement within the Patagonian Batholith identified by Hervé *et al.* (2007). Inset locates this figure in southernmost South America. Box indicates the location of Fig. 2a.

structural relationships, detailed petrology and mineral equilibria modelling that build on previous work (Nelson *et al.*, 1980; Kohn *et al.*, 1993, 1995) and recently published U–Pb zircon data from rocks in nearby areas (Barbeau *et al.*, 2009; Hervé *et al.*, 2010; Klepeis *et al.*, 2010).
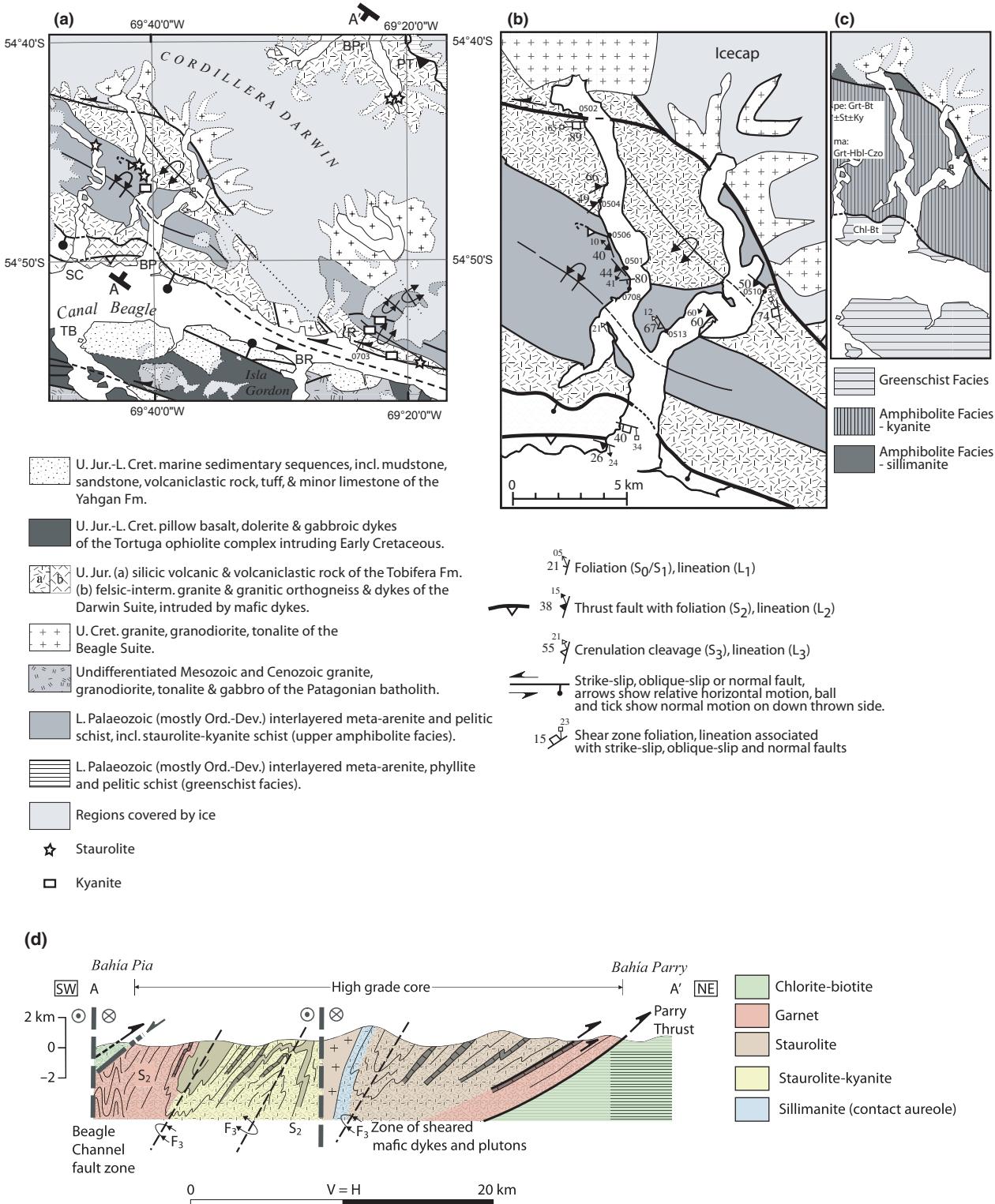
(a)

69°40'0"W   A' 69°20'0"W

54°40'S   BPr   54°40'S
PT

C O R D I L L E R A   D A R W I N

54°50'S   54°50'S

SC

BP

Canal Beagle   A

TB

R   0703

BR

Isla Gordon

69°40'0"W   69°20'0"W

U. Jur.-L. Cret. marine sedimentary sequences, incl. mudstone, sandstone, volcaniclastic rock, tuff, & minor limestone of the Yahgan Fm.

U. Jur.-L. Cret. pillow basalt, dolerite & gabbroic dykes of the Tortuga ophiolite complex intruding Early Cretaceous.

U. Jur. (a) silicic volcanic & volcaniclastic rock of the Tobifera Fm. (b) felsic-interm. granite & granitic orthogneiss & dykes of the Darwin Suite, intruded by mafic dykes.

U. Cret. granite, granodiorite, tonalite of the Beagle Suite.

Undifferentiated Mesozoic and Cenozoic granite, granodiorite, tonalite & gabbro of the Patagonian batholith.

L. Palaeozoic (mostly Ord.-Dev.) interlayered meta-arenite and pelitic schist, incl. staurolite-kyanite schist (upper amphibolite facies).

L. Palaeozoic (mostly Ord.-Dev.) interlayered meta-arenite, phyllite and pelitic schist (greenschist facies).

Regions covered by ice

☆ Staurolite

☐ Kyanite

(b)

Icecap

0502
ISP
89
66
0504
10
40   0506
44   0501
41   80
0708
12   60   0510
21   67   60   74
0513

40
34
26   24

0   5 km

(c)

pe: Grt-Bt ±St±Ky

ma: Grt-Hbl-Czo

Chl-Bt

Greenschist Facies

Amphibolite Facies - kyanite

Amphibolite Facies - sillimanite

$\overset{05}{21}$ Foliation (S_0/S_1), lineation (L_1)

$\overset{15}{38}$ Thrust fault with foliation (S_2), lineation (L_2)

$\overset{21}{55}$ Crenulation cleavage (S_3), lineation (L_3)

Strike-slip, oblique-slip or normal fault, arrows show relative horizontal motion, ball and tick show normal motion on down thrown side.

$\overset{23}{15}$ Shear zone foliation, lineation associated with strike-slip, oblique-slip and normal faults

(d)

Bahía Pia   Bahía Parry

SW A   High grade core   A' NE

2 km   Parry Thrust
0
−2   S_2

Beagle Channel fault zone   F_3   F_3   S_2   F_3 Zone of sheared mafic dykes and plutons

0   V = H   20 km

Chlorite-biotite

Garnet

Staurolite

Staurolite-kyanite

Sillimanite (contact aureole)

Fig. 2. (a) Structural map of a region within the Cordillera Darwin. A and A′ locate the cross-section in (d). Sample 0703 located on map. SC: Seno Cerrado, TB: Bahía Tres Brazos, BP: Bahía Pia, BR: Bahía Romanche, R: Ventisquero Roncagli; BPr: Bahía Parry; PT: Parry Thrust. After Klepeis *et al*. (2010). (b) Structural map of Bahía Pia with fault orientations and site locations discussed in the text. (c) Location of diagnostic metamorphic mineral assemblages found in Bahía Pia, m: mafic protolith, pe: pelitic protolith. (d) Cross-section with metamorphic isograds from Bahía Pia to Bahía Parry, with rock type patterns as given in legend of (a). After Klepeis *et al*. (2010).

REGIONAL SETTING

Cordillera Darwin forms part of the Fuegian Andes, which comprise a comparatively topographically subdued portion of the Andean mountain chain. The geology of this belt has been divided (after Kranck, 1932; Nelson *et al.*, 1980; Dalziel, 1981; Winslow, 1982; Suárez *et al.*, 1985) into four main elements: (i) pre-Late Jurassic Gondwanide elements; (ii) the Late Jurassic to Early Cretaceous Rocas Verdes marginal basin (Dalziel *et al.*, 1974; Bruhn *et al.*, 1978; Allen, 1982; Hanson & Wilson, 1993); (iii) Cretaceous to Cenozoic plutonic rocks of the Patagonian batholith, interpreted as the root of a Pacific magmatic arc; and (iv) a fold and thrust belt comprising uppermost Cretaceous to Palaeogene sedimentary rocks of the Magallanes and Malvinas foreland basins (Fig. 1).

Palaeozoic to Jurassic metasedimentary rocks and metavolcanics deposited along the proto-Pacific Gondwana margin and interpreted to form much of Cordillera Darwin (Fig. 1) have widespread equivalents in, for example, Antarctica (Dalziel & Elliot, 1971; Stump, 1995), South Africa (de Wit, 1977) and the Lachlan Fold belt of eastern Australia (Foster & Gray, 2000), although metasedimentary rocks forming a basement to Cordillera Darwin differ in provenance to those underlying the Magallanes foreland basin (Hervé *et al.*, 2010). In the Fuegian Andes, care is required to separate pre-Mesozoic orogenic features from those related to their tectonic reworking during closure of the Rocas Verdes marginal basin (Nelson *et al.*, 1980; Kohn *et al.*, 1993). Detrital zircon age patterns for samples taken from areas focussed on for work in this paper (Bahía Pia) have a range of peaks the most prominent of which is Cambro-Ordovician in age, indicating their protoliths are Palaeozoic (Hervé *et al.*, 2010).

During the Early and Middle Jurassic, voluminous basaltic and less abundant rhyolitic volcanism erupted onto Gondwana in its incipient stages of dispersal (Encarnación *et al.*, 1996; Duncan *et al.*, 1997; Minor & Mukasa, 1997). In Patagonia and the Antarctic Peninsula, Jurassic silicic volcanic rocks, basal breccia, conglomerate and fossiliferous shale and sandstone, of the Tobifera Formation (Natland *et al.*, 1974; Gust *et al.*, 1985; Hanson & Wilson, 1991; Pankhurst *et al.*, 2003; Calderón *et al.*, 2007) record this phase of crustal extension. These felsic volcanics and related granitoids in Patagonia are interpreted to reflect the later stages (175–160 Ma) of a plate margin migration of magmatism related to continental break-up (Pankhurst *et al.*, 2000). Widespread basaltic and gabbroic dyke swarms in pre-Jurassic 'basement' rocks record further crustal extension, correlated with Early Cretaceous pillow basalts and hyaloclastite interlayered with chert and siltstone that record the opening of the Rocas Verdes marginal basin (Dalziel *et al.*, 1974; Stern *et al.*, 1992; Stern & de Wit, 2003) between *c.* 152 and 142 Ma (Calderón *et al.*, 2007). Interbedded shale and silt-dominated sequences conformably overlie silicic pyroclastic deposits and mafic pillow basalts (Allen, 1982; Fuenzalida & Covacevich, 1988; Fildani & Hessler, 2005). This sedimentary fill includes rocks of the Zapata and Yahgan Formation, and equivalents (Dalziel & Elliot, 1971; Halpern & Rex, 1972; Dott *et al.*, 1982; Wilson, 1991; Olivero & Martinioni, 2001) that might represent turbidite deposits (Fuenzalida & Covacevich, 1988). These units thicken to the southeast from the Ultima Esperanza region (51.5°S; Fig. 1), reflecting a widening of the back-arc basin with distance south. These units conformably overlie the Tobifera Formation.

Compression and crustal shortening beginning in the Late Cretaceous resulted in a series of events that mark the onset of Andean orogenesis in Patagonia (Dott *et al.*, 1977; Dalziel, 1981; Wilson, 1991). These include the formation of the flexural Magallanes foreland basin (Natland *et al.*, 1974; Dott *et al.*, 1982; Winslow, 1982; Biddle *et al.*, 1986; Wilson, 1991; Fildani & Hessler, 2005), and the Magallanes fold-thrust belt intercalating components of the Palaeozoic basement and mafic floor and sedimentary fill of the Rocas Verdes basin (Dalziel *et al.*, 1974; Nelson *et al.*, 1980; Calderón *et al.*, 2007; Klepeis *et al.*, 2010). Fine to medium-grained sandstones that overlie rift basin sedimentary rocks of the Rocas Verdes basin mark the beginning of foreland basin sedimentation. These include sequences of the Punta Barrosa Formation that conformably overlie the Zapata Formation (Wilson, 1991; Fildani & Hessler, 2005). Detrital zircon spectra suggest that the Punta Barrosa Formation is no older than *c.* 92 Ma, in the Ultima Esperanza region (Fildani *et al.*, 2003). In Tierra de Fuego, the equivalent units may be somewhat younger (McAtamney *et al.*, 2009). Crustal shortening in the Magallanes foreland propagated northwards, terminating in the Eocene (Alvarez-Marrón *et al.*, 1993; Ghiglione & Ramos, 2005; Barbeau *et al.*, 2009; Gombosi *et al.*, 2009).

Rocks now exposed in Cordillera Darwin experienced convergence-related burial followed by exhumation (Kohn *et al.*, 1995), contemporary with the development of the Magallanes foreland basin and thrust belt (Nelson *et al.*, 1980; Halpern, 1973; Cunningham, 1995; Klepeis *et al.*, 2010). Kyanite–staurolite-bearing assemblages reflect metamorphic conditions of 580–630 °C and 7–12 kbar (Kohn *et al.*, 1993; below). Fission-track thermochronology (Nelson, 1982) and $^{40}Ar/^{39}Ar$ cooling ages (Kohn *et al.*, 1995) reveal an initial stage of cooling (from 550 to 325 °C) and exhumation from *c.* 90 to 70 Ma. A second stage of cooling (< 250 °C) and further exhumation from the Palaeocene to the Middle Eocene (Kohn *et al.*, 1995; Barbeau *et al.*, 2009; Gombosi *et al.*, 2009).

Granite, dolerite and gabbro intruded Palaeozoic basement, and rift-related sequences including the Tobifera Formation and sedimentary fill of the Rocas

Verdes basin (Nelson *et al.*, 1980; Suárez *et al.*, 1985; Cunningham, 1994; Klepeis *et al.*, 2010). Two granitic suites have been observed in southern Cordillera Darwin: (i) the Late Jurassic Darwin suite (Nelson *et al.*, 1980; Hervé *et al.*, 1981, 2010); and (ii) the Late Cretaceous Beagle suite (Nelson *et al.*, 1980; Hervé *et al.*, 1984; Klepeis *et al.*, 2010). The granite suites are a local manifestation of the south Patagonian batholith, which records *c.* 150 Myr of subduction related magmatism (Hervé *et al.*, 2007). In Cordillera Darwin, gabbroic sills and dolerite dykes represent magmatism that accompanied the opening of the Rocas Verdes back-arc basin (Nelson *et al.*, 1980; Cunningham, 1994). Low-grade remnants of this magmatism now form the Sarmiento and Tortuga Ophiolite complexes (Fig. 1; Suárez & Pettigrew, 1976; Stern, 1980; Allen, 1982; Calderón *et al.*, 2007). Pre-Jurassic basement rocks retain evidence for a foliation that predates emplacement of the Darwin Granite Suite (Nelson *et al.*, 1980) and may be Palaeozoic in age, but pre-Jurassic metamorphic conditions evidently did not exceed lower greenschist facies (Nelson *et al.*, 1980; Kohn *et al.*, 1993, 1995). High-grade metamorphic fabrics in eastern Cordillera Darwin are cut by the Beagle Suite (Nelson *et al.*, 1980; Moore, 1990; Kohn *et al.*, 1995), which appears to have been emplaced over a period between *c.* 86 and 70 Ma (Klepeis *et al.*, 2010; S. A. Thomson & K. A. Klepeis, unpublished U–Pb zircon data).

Greenschist facies strike-slip and normal faults occur along the Beagle Channel (Dalziel & Brown, 1989; Cunningham, 1993, 1995). These cut all upper amphibolite facies fabrics and plutons in Cordillera Darwin (Klepeis *et al.*, 2010), and record the effects of strike-slip faulting that has occurred from at least the late Tertiary to the present (Gombosi *et al.*, 2009).

BAHÍA PIA AND VENTISQUERO RONCAGLI

Multiply deformed amphibolite facies metapelitic schist occurs interlayered with mafic and felsic orthogneiss in Bahía Pia (Nelson *et al.*, 1980), and in the vicinity of Ventisquero Roncagli (Cunningham, 1995). Kohn *et al.* (1993, 1995) characterized variations in metamorphic grade through central Cordillera Darwin based on the occurrence of a series of index minerals, specifically chlorite–biotite, garnet, kyanite, staurolite and/or sillimanite. Following early work by Nelson *et al.* (1980), Kohn *et al.* (1993) identified a pronounced metamorphic discontinuity across the north-west arm of the Beagle Channel – whereas kyanite-grade schists occur north of the channel, only chlorite–biotite-grade schists were identified in similar lithologies to the south (Fig. 2a,c).

Bahía Pia exposes north-west-trending, interlayered amphibolite facies schists, felsic and mafic orthogneiss, all in fault contact with chlorite–biotite grade (after Kohn *et al.*, 1993), south-dipping Tobifera Formation

rocks (Fig. 2; Table 1). Recent U–Pb dating of detrital zircon grains in staurolite–kyanite-bearing schists (Hervé *et al.*, 2010) has confirmed a long-standing interpretation based on Rb–Sr whole-rock data (Hervé *et al.*, 1981) of Palaeozoic protoliths. These schists are commonly referred to as 'basement' to the Rocas Verdes series (Nelson *et al.*, 1980; Hervé *et al.*, 1981). The oldest foliation that can be identified in the schists is a layer-parallel foliation (S1) cut by *c.* 160 Ma felsic orthogneiss (Fig. 3a) of the Darwin Suite (Klepeis *et al.*, 2010). S1 is commonly interpreted as preserving evidence for pre-Jurassic orogeny, interpreted to precede the emergence of the Andean mountain chain (Hervé *et al.*, 1981). In the Bahía Pia amphibolite facies schists, S1 contains intrafolially folded quartz veins and laminae and it seems likely that S1 is a composite fabric that includes pre-Jurassic and Cretaceous components. This interpretation is compatible with that of Nelson *et al.* (1980).

Felsic orthogneiss of the Darwin Granite Suite is cut by numerous mafic dykes (Fig. 3a,b), which are interpreted as being equivalent to the Tortuga and Sarmiento Ophiolite (Calderón *et al.*, 2007). Amphibolite facies assemblages in the felsic orthogneiss and recrystallized mafic dykes define a moderately (~60°) south-west-dipping S2 foliation (Fig. 3c,d), which includes a down-dip mineral lineation and is commonly a spaced crenulation cleavage in graphitic schist (Fig. 3e). Silicic schists mainly contain S1 folia, tightly folded (Fig. 3c) or transposed into S2 (Fig. 3d,e). Garnet in both metapelitic schists and metamorphosed dykes may preserve fine-grained S1 inclusion trails oblique to S2 (below), supporting the interpretation that S1 is a composite age fabric.

In fiords further west (Seno Garibaldi, Seno Ventisquero), shallowly dipping S2–L2 fabrics and thrust faults that juxtapose 'basement' schists and 'cover' units are interpreted to record the north-east-directed thrusting of the 'basement' nappe onto the larger South American craton (e.g. Nelson *et al.*, 1980). In Seno Parry, to the north of Bahía Pia, north-east directed thrusting places amphibolite facies orthogneiss over greenschist facies metapelites along the Parry Thrust (Fig. 2a,d), which forms the northern limit of high-grade metamorphic rocks (Klepeis *et al.*, 2010). Lower grade Tobifera rocks in southern Bahía Pia contain a fabric interpreted as equivalent to S2 in amphibolite facies schists of northern Bahía Pia and Ventisquero Roncagli area (Fig. 2a,b).

S2 is deformed by macroscopic, reclined F3 folds with a north-east dipping axial plane that deform all metamorphic fabrics but which lack pervasive fabric development (Fig. 2d). These folds are interpreted to reflect the post-metamorphic back-folding of a north-east vergent nappe pile (Nelson *et al.*, 1980). S1 and S2 fabrics, and F3 folds are all cut by *c.* 86–70 Ma felsic plutons of the Beagle Suite (Kohn *et al.*, 1995; Klepeis *et al.*, 2010) which have contact aureoles with weakly

Table 1. Timing of major events and formation of fabrics in Cordillera Darwin.

Time (Ma)	Event	Foliation	Nature	Lineation	Mineral assemblage	Reference
Palaeozoic to Jurassic	Deposition of 'basement' rocks					Hervé et al. (1979, 1981, 2010)
Pre-Late Jurassic	Pre-Darwin Granite orogeny	S1	Intrafolial		Inferred greenschist	Nelson et al. (1980)
164 ± 1	Darwin Granite; U–Pb zircon					Mukasa & Dalziel (1996)
157 ± 7	Rb–Sr					Hervé et al. (1981)
159 ± 1	U–Pb on zircon; rhyolite dyke					Hervé et al. (2010)
172 ± 1	U–Pb on zircon from Tobifera volcanic					Pankhurst et al. (2000)
163 ± 2	U–Pb on zircon from Tobifera sandstone Verdes basin)					Hervé et al. (2010)
152–142	Mafic dyke swarm (related to formation of Rocas Verdes basin)					Hervé et al. (1979, 1981), Nelson et al. (1980), Calderón et al. (2007)
	Penetrative fabric development Underthrusting (Pia); obduction (Seno Ventisquero, western Beagle Channel)	S1			Amphibolite facies Pelite: Grt–Bt–Ms ± Ep*	Klepeis et al. (2010); this paper
86 ± 1	Early Beagle Suite granite that cuts obduction structures				Mafic: Grt–Hbl–Czo–Pl	Klepeis et al. (2010)
73 ± 1	Staurolite–kyanite growth Patchy recrystallization of garnet (exhumation of Cordillera Darwin)	S2	SE-trending, folded Dips SW 65°	Down dip	Grt–Bt–Ky–St	Monazite; this paper
90 ± 2, 69 ± 1	Beagle Granite; U–Pb zircon				Bt–Sil–Ms migmatites in contact aureoles	Mukasa (in Kohn et al., 1995)
c. 70	U–Pb zircon					S. Thomson & K. Klepeis (unpublished data)
73–65 Ma	Hbl, Kfs Ar–Ar cooling ages Continued uplift of Cordillera Darwin					Kohn et al. (1995)
	Macroscopic overturned folds	F3	NW-trending			Klepeis et al. (2010)
Palaeogene or younger	Strike slip, oblique slip, normal faults					Gombosi et al. (2009)

*Mineral symbols used here and elsewhere are after Kretz (1983), extended by Bucher & Frey (1994).

deformed sillimanite–garnet–biotite migmatites in the northernmost and easternmost portions of Bahía Pia (stations 0502, 0510, Fig. 2c). Similar aureoles with metapelitic assemblages that include sillimanite, staurolite, garnet and biotite were identified in Seno Romanche, south of the Beagle Channel. All rocks are cut by strike-slip and oblique-slip normal faults and shear zones (Fig. 2a) that are possibly as old as the Miocene (Klepeis, 1994b; Klepeis & Austin, 1997; Lodolo et al., 2003; Ghiglione & Ramos, 2005; Barbeau et al., 2009) and control much of the current topography.

The outlet valley and ridges adjacent to Ventisquero Roncagli include staurolite–kyanite schists and orthogneiss (Cunningham, 1995) that represent along-strike equivalents of the schists exposed in Bahía Pia. Metamorphic grade and structural relationships record a history similar to that of the rocks in Bahía Pia (Fig. 2). Cunningham (1995) interpreted a macroscopic antiform defined successively by garnet, kyanite–staurolite, garnet and biotite zones on a ridge parallel to the valley. This succession corresponded, respectively, to orthogneiss, schist and orthogneiss units in our field traverses, with mineral zones mostly reflecting variations in lithology, not grade. The schists include kyanite–garnet–staurolite-bearing assemblages that assist with the interpretation of the Bahía Pia assemblages.

PETROGRAPHY

The focus of this paper involves amphibolite facies basement schists and orthogneiss to the north of Tobifera exposures in Bahía Pia, and equivalent schists forming a prominent ridge to east of Ventisquero Roncagli (Fig. 2a). This paper concentrates on complex garnet textures in metapelitic schists, building on the work of Nelson et al. (1980) and Kohn et al. (1993, 1995). Tobifera exposures in Bahía Pia are much finer grained (minerals 0.1–0.2 mm) than the basement schists, being formed from felsic schists comprising chlorite, biotite, titanite, plagioclase and quartz interlayered with mafic schists comprising actinolite, chlorite, biotite, epidote, plagioclase and quartz. Garnet was not observed in these rocks, and grain size is an order of magnitude smaller than in the amphibolite facies schists.

Most basement schists in Bahía Pia are felsic, comprising plagioclase–quartz-rich layers alternating with muscovite–biotite layers on a cm-scale (Fig. 3e). Grains are mostly 1–2 mm across. Ilmenite and less abundant rutile occur in either laminae, with or without garnet. Micaceous laminae may range in size up to decimetre or metre-scale, where they additionally contain garnet, staurolite and kyanite. A distinctive layer of graphite-rich aluminous schist is continuous across the two arms of Bahía Pia; most aluminous
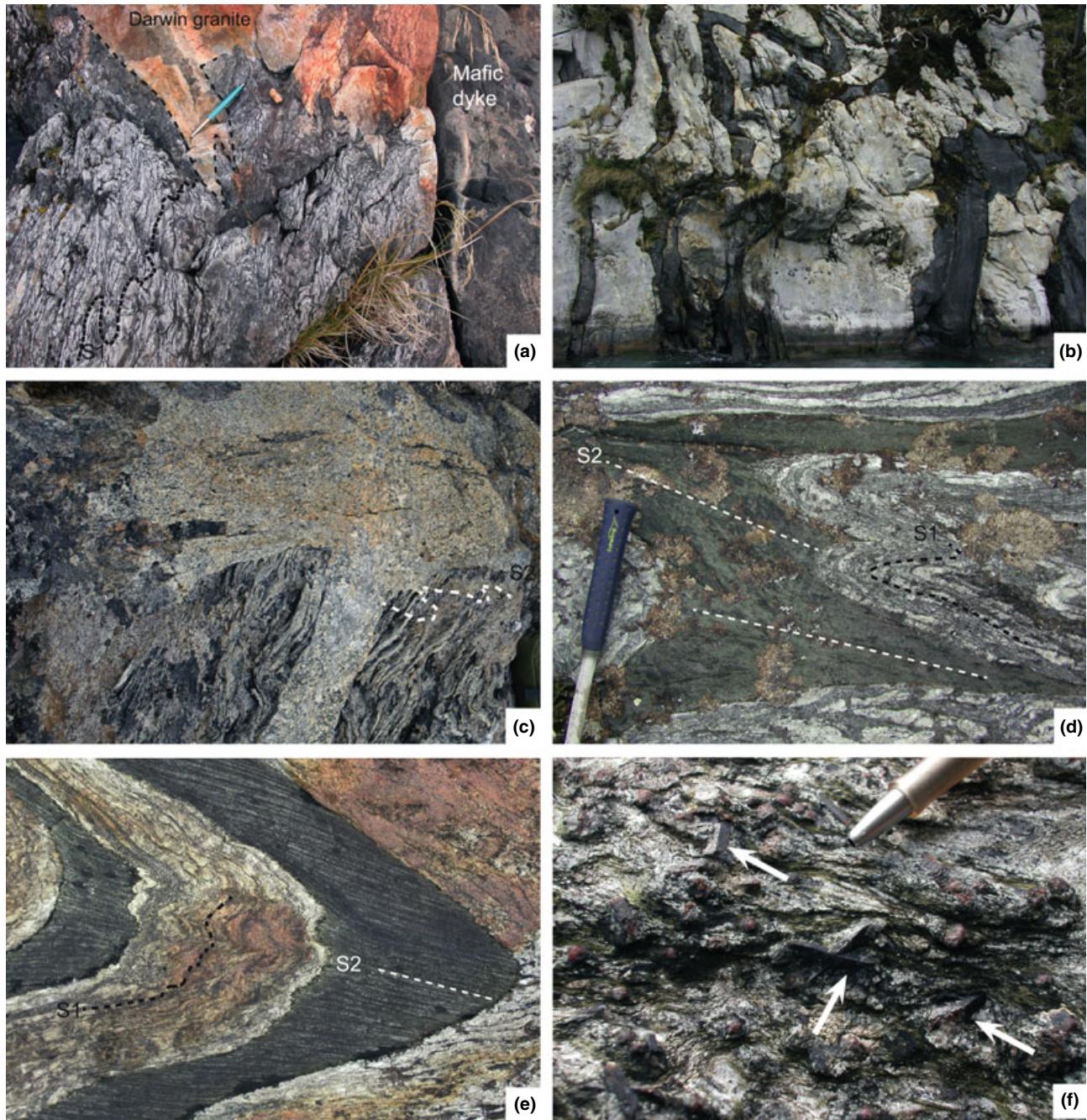
Fig. 3. (a) Composite S1 in Palaeozoic basement, cut by *c*. 160 Ma Darwin granite, which contains S2. Bahía Pia site 0502. (b) Deformed *c*. 145 Ma mafic dyke swarm cutting Darwin granite. Bahía Pia site 0504. (c) Dykes of Beagle Granite cutting S3 in Palaeozoic basement schists. Roncagli area. (d) Metamorphosed and deformed mafic dykes that preserve S2 in Palaeozoic schists that preserve S1 and S2 foliations. Bahía Pia site 0506. (e) Transposition of S1 foliation into S2 in carbonaceous schist in Palaeozoic basement. Bahía Pia site 0501. (f) Cruciform twinning in post-S1 staurolite in Grt–St–Ky–Bt schist. Bahía Pia site 0513.

minerals in this layer have abundant fine-grained graphite inclusions. The penetrative foliation in most samples is S2, which largely comprises a spaced crenulation of S1 in the graphite-rich schists (Fig. 3e).

Centimetre-scale garnet grains at both Bahía Pia and Ventisquero Roncagli may contain curved or folded inclusions of S1 plagioclase, epidote, quartz, rutile, ilmenite, muscovite and/or biotite, with or without graphite (Figs 4a–d & 5a,b). Individual S1 grains are commonly < 0.1 mm across. Curved and folded S1 inclusion trails are consistent with garnet having grown syn-tectonically with respect to D2 (Fig. 4d).

In comparison with other textures described below, garnet with distinct S1 inclusion trails has a clear habit, locally clouded by graphite inclusions. Cruciform twins of staurolite (Fig. 3f) have planar S2 quartz, rutile and ilmenite inclusions, at a high angle to curved S1 inclusions in garnet (Figs 4a & 5c), consistent with staurolite growth late in, or after, the development of S2 (also Cunningham, 1994). Kyanite also has inclusions of S2 rutile and ilmenite, consistent with it having formed at the same time as staurolite. S2 is the dominant foliation observed within the matrix, and is primarily defined by biotite, muscovite and quartz (Fig. 4a). Minerals involved in the S2 paragenesis are garnet rims, staurolite, kyanite, biotite, muscovite, rutile, ilmenite, plagioclase and quartz.

Garnet in amphibolite facies schists of Bahía Pia may preserve complex textures, which include patches and core or rim domains of turbid garnet intergrown with comparatively coarse-grained (0.5–1 mm diameter) randomly oriented biotite, muscovite, plagioclase, ilmenite, rutile, quartz, monazite and zircon. Such grains with 'patch' textures of turbid garnet may occur adjacent to clear garnet grains that preserve folded S1 inclusions trails (Fig. 5d). Inclusions ~1–2 μm across cause the turbid appearance to the garnet patches; their small size hampers identification. Turbid garnet may occur as comparatively small parts of otherwise clear garnet grains (Fig. 5c), form most of a grain (Fig. 5e), or anything in between (Fig. 5f). At an incipient stage of development of this texture (e.g. Fig. 5c) isolated coarse-grained mineral inclusions, one to two orders of magnitude larger than those forming S1 inclusion trails, occur apparently entirely surrounded by garnet, but with turbid garnet adjacent the large mineral inclusions (Fig. 5c). Garnet that is dominantly turbid commonly has fracture traces that connect isolated large inclusions (Figs 4e & 5h), or isolated patches of incipient turbid garnet, to the host grain boundaries (Fig. 5c). In cases, atoll-like structures are developed (Fig. 6), comprising a core or rim domain of turbid garnet intergrown with large randomly oriented minerals, enclosed by a mantle of 'clear' garnet that may preserve fine-grained S1 inclusion trails. Large syn- to post-S2 staurolite and kyanite porphyroblasts commonly occur adjacent to garnet grains with the patchy turbid textures (Figs 4e & 5f). Garnet with turbid patches truncates S1 inclusions trails (e.g. Fig. 5d), but many recrystallized grain cores have ambiguous timing relationships with respect to the matrix S2 foliation. On the basis of S1 truncations at turbid-clear boundaries, and our inferred relationship between the development of the turbid garnet and staurolite and kyanite growth, we infer that the turbid garnet formed during and after the development of S2.

Curved inclusion trails similar to those in clear garnet from Bahía Pia occur in the Ventisquero Roncagli samples, but garnet from this area appears to lack the development of turbid textures (Fig. 5a). At both Bahía Pia and Ventisquero Roncagli, garnet, biotite, staurolite and kyanite in the metapelitic schists are partially to completely pseudomorphed by randomly orientated intergrowths of chlorite and muscovite (Fig. 4c). Garnet in metabasite is commonly partially retrogressed to randomly oriented chlorite. Felsic orthogneiss interlayered with metapelitic schist at Bahía Pia comprises S2 plagioclase, microcline, quartz, biotite and ilmenite with or without garnet and/or muscovite. Recrystallized mafic dykes comprise S2 hornblende, plagioclase, biotite and ilmenite, with or without garnet, rutile, epidote and titanite (grains 1–2 mm across). Garnet may have oriented inclusions of epidote, titanite and plagioclase, indicating complexity in the development of S2 and/or age of protolith(s) (Fig. 4f).

At Bahía Pia locations 0502 and 0510, migmatite containing sillimanite, plagioclase, biotite and ilmenite, with or without garnet, as well as garnet-bearing metasedimentary schist similar to that described above, have coarse-grained intergrowths of muscovite, biotite and fibrolitic sillimanite (Fig. 4g) that cut S2 and are weakly aligned with a late shear fabric. Randomly oriented chlorite partially pseudomorphs biotite, garnet and sillimanite. Similar, weakly foliated textures were found in Seno Romanche (0709) south of the Beagle Channel, where fine-grained (0.5 mm) metasedimentary rocks include calc-schist layers of plagioclase, hornblende, biotite, ilmenite, epidote and quartz with or without diopside. These occur interlayered with metapelitic layers comprising plagioclase, biotite, garnet, quartz, ilmenite and fibrolitic sillimanite. Another finely layered rock at the same location comprises: (i) comparatively coarse-grained (1 mm) metapelitic layers of garnet, biotite, muscovite, staurolite, sillimanite, ilmenite and quartz interlayered with; (ii) metapsammite layers comprising plagioclase, quartz, biotite, muscovite and ilmenite. These are the first reported occurrences of garnet and sillimanite south of the Beagle Channel, and are interpreted as contact effects of Beagle Suite plutons on metasedimentary hosts at both Bahía Pia and Seno Romanche. Garnet in the samples from Bahía Pia aureoles lacks the patch textures evident outside the aureoles.

GARNET MINERAL CHEMISTRY AND RAMAN ANALYSIS

The main features of the mineral chemistry are presented in Kohn *et al.* (1993, 1995), with detail relevant to the samples used for this work summarized in Table 2. Analyses were performed on the Cameca SX-50 Camebax microprobe housed at the University of New South Wales, operating with an accelerating voltage of 15 kV, a beam width of 1–5 μm and PAP data reduction techniques supplied by the manufacturer. For the purpose of analysing the complex garnet textures and applying the mineral equilibria modelling described below, this paper concentrates on garnet relationships in key metapelitic samples from Bahía Pia (0708) and the ridge east of Ventisquero Roncagli (0703).

A detailed compositional profile was collected through a garnet grain in sample 0703 at a high angle to S1 (Fig. 5g). The profile extends from a spessartine–grossular-rich core to a comparatively pyrope–almandine-rich rim (Fig. 7a). An inner bell-shape defined by both grossular and spessartine is similar to the interpreted growth zoning used by Kohn et al. (1993) to recover a prograde path for Cordillera Darwin involving 500–620 °C at 6–9 kbar. A broad outer mantle of comparatively spessartine–grossular-poor garnet (left side of Fig. 7a) reflects areas that have inclusions aligned with S2 (Fig. 5g), matched by a compositionally similar, narrow zone on the other grain boundary.

A traverse made through a garnet grain from Bahía Pia sample 0708 with turbid patches (Fig. 5h) has complex chemical zoning (Fig. 7b). The pattern is similar for an orthogonal traverse that is oblique to the foliation (not shown). Spessartine content varies smoothly from core to rim in a fashion similar to that in sample 0703. However, grossular, pyrope and almandine contents in the grain vary complexly, in patterns coupled with analyses collected from either clear or turbid sections of the garnet grain. Turbid portions of the garnet grain have lower grossular and higher pyrope content than clear adjacent portions of the grain. Turbid areas within the garnet grain have similar pyrope content to that near grain boundaries (Fig. 7b).

Raman spectroscopy was performed on the garnet grains using an excitation line of 514 nm. Spectra are broadly similar between the turbid and clear areas and are dominated by garnet bond peaks (after Bersani et al., 2009), but significant differences are observed (Fig. 7c). Turbid garnet has a broad peak between 3300 and 3700 cm^{-1} lacking in spectra collected from clear garnet, associated with the stretching mode of the O–H bond of water, with small, superimposed peaks indicating impurities of aqueous solution (Dubessy et al., 2001). The strongest band in both spectra is the garnet Si–O stretching mode at $\sim$910 cm^{-1} (Bersani et al., 2009). This band increases in wave number from $\sim$906 to 917 cm^{-1} with the change from grossular to spessartine–pyrope rich garnet. Both spectra show a series of peaks from 2840 to 3100 cm^{-1} consistent with the presence of hydrocarbons (Wörner et al., 1993; Dubessy et al., 2001; Fan et al., 2004).

Maps of Mn, Mg and Ca X-ray intensity were also collected over part of patchily recrystallized garnet texture in sample 0506 (Fig. 6). Semi-quantitative cation proportions were then calculated using matrix corrections and analyses of garnet isolated from other minerals by using a mixture of element thresholds (Clarke et al., 2001). Clear garnet has high, variable grossular content, whereas turbid garnet is rich in pyrope, similar to relationships in sample 0708. A narrow rim of the garnet grain in sample 0506 has spessartine, pyrope and grossular contents that match its turbid core. Turbid parts of the garnet grain have higher, homogeneous spessartine contents in contrast with that in the clear domains, resulting in garnet with grossular-rich clear regions and pyrope–spessartine-rich turbid regions (Fig. 6).

GEOCHRONOLOGY

Three sensitive high-resolution ion microprobe (SHRIMP) mounts were prepared from segments of two thin sections of garnet-bearing metapelitic schist samples 0501 (mounts Z5490 & Z5491) and 0708 (mount Z5495) from Bahía Pia, for the purpose of U–Th–Pb monazite dating. Monazite was analysed in situ within selected areas of the polished thin sections, recast into epoxy discs together with reference monazite grains (44069). Reflected and transmitted light photomicrographs were prepared for navigation, as were Scanning Electron Microscope (SEM) back-scattered and secondary electron (BSE) images of the monazite internal structure (Fig. 8). The images were used to ensure that the $\sim$20 μm SHRIMP analysis spot was wholly within a single age component within the sectioned grains.

The U–Th–Pb analyses were made using SHRIMP II at the Research School of Earth Sciences, The Australian National University, Canberra, Australia following procedures given in Williams (1998, and references therein). As the monazite grains were expected to be, and are, Cretaceous in age, no energy filtering was applied to the extracted secondary ion beam. As such, common Pb correction was made using the measured $^{207}Pb/^{206}Pb$ ratios as outlined by Williams (1998). Each analysis consisted of six scans through the mass range, with the 44069 reference monazite grains analysed after each group of three unknown analyses. Data were reduced using the SQUID Excel Macro of Ludwig (2001). The Pb/U ratios have been normalized relative to a value of 0.0668 for the 44069 reference monazite, equivalent to an age of 424.9 Ma (see Aleinikoff et al., 2006). Uncertainty in the U–Pb calibration was 1.19%, 0.62% and 0.45% for the three polished thin sections analysed, Z5495, Z5490 and Z5491, respectively.

Uncertainties given for individual analyses (ratios and ages) are at the one sigma level (Table 3). Tera & Wasserburg (1972) concordia plots, probability density plots with stacked histograms, and weighted mean $^{206}Pb/^{238}U$ age calculations (Fig. 9) were carried out using ISOPLOT/EX (Ludwig, 2003). Weighted mean $^{206}Pb/^{238}U$ ages (^{207}Pb corrected) were calculated, including addition of the U/Pb ratio calibration uncertainty (added in quadrature) and the uncertainties are reported as 95% confidence limits.

Thirteen analyses were performed on monazite grains in mount Z5490, 13 on mount Z5491 and 11 on mount Z5495. Monazite grains in the samples were all located within the quartz–mica-rich domains outside large garnet porphyroblasts (Fig. 8a,c); no monazite was found in any garnet examined under the SEM. All observed monazite is aligned with S2 in the matrix, and occurs in contact with biotite, muscovite, plagioclase and quartz. Monazite grains range in size from $\sim$20 to
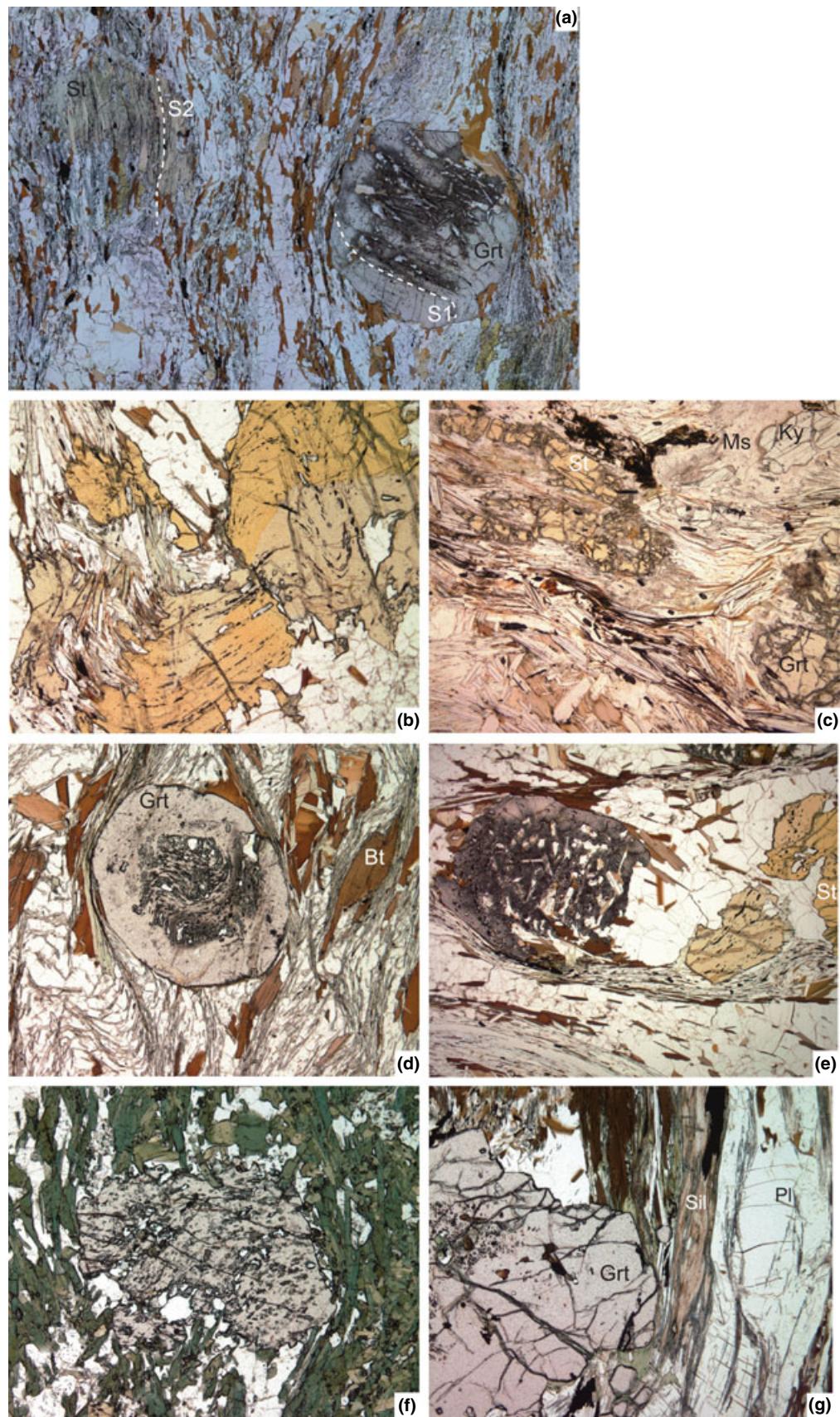
150 μm, and pleochroic halos are common in adjacent minerals. Xenotime also occurs in the quartz–mica-rich domains of the rock, and inside garnet. Monazite grains are all anhedral to subhedral, and, on the basis of SEM imaging, lack chemical zoning (Fig. 8b). All monazite is inferred to be metamorphic in origin, with no age or zoning patterns that might reflect inherited grains; the metamorphic event that produced the monazite is inferred to be the same as the one that formed the dominant S2 foliation.

Ages from the grains in each sample were generally consistent and gave an overall age of 72.6 ± 1.1 Ma. Some slightly older ages between c. 78 and 74 Ma from mount Z5495 were interpreted to be a consequence of machine U/Pb ratio calibration anomalies arising from the relative large expanse of this particular SHRIMP mount, the older analyses having being made near the edge of this probe mount. Monazite grains from the other two mounts agree to within analytical uncertainty.

MINERAL EQUILIBRIA MODELLING AND *P–T* PATH

Pseudosections show the stable multivariant equilibria in a given chemical system for a specific rock composition or rock compositional vector (Powell *et al.*, 1998). *P–T* pseudosections allow observed assemblages to be quantitatively constrained for a specified rock composition (e.g. Powell *et al.*, 1998; White *et al.*, 2002). The chosen model chemical system should describe the major chemical components in the rock system as fully as possible. The model system of Na_2O–CaO–K_2O–FeO–MgO–Al_2O_3–SiO_2–H_2O–TiO_2–Fe_2O_3 (NCKFMASHTO) was chosen to calculate phase relationships and reaction processes in the Cordillera Darwin schists. This system represents the combination of the NCKFMASH model of White *et al.* (2001) and KFMASHTO model of White *et al.* (2002) as outlined in White *et al.* (2003). Though important, MnO was not included in the model system because refined *a*-X models are yet to be constructed for minerals other than garnet. The main effect of including MnO in the model system is to expand the garnet-bearing field, with small modes of spessartine-rich garnet appearing at lower *P–T* conditions than shown in NCKFMASHTO pseudosections.

Calculations were undertaken using THERMOCALC (version 3.32; Powell & Holland, 1988) with the internally consistent thermodynamic data set of Holland & Powell (1990; data set created on 22 November 2003). Calculations involved the phases chlorite, quartz, ilmenite, rutile, titanite, epidote, garnet, plagioclase, K-feldspar, biotite, muscovite, kyanite, sillimanite, silicate melt and water. Activity–composition relationships of phases follow White *et al.* (2003). The bulk rock composition used in the modelling could not be determined directly from X-ray fluorescence (XRF) whole-rock analyses, due to the pronounced zoning in garnet and therefore the sequestering of elements (e.g. Marmo *et al.*, 2002). Instead, representative microprobe data of the main rock-forming S2 minerals in 0708b were weighted according to mineral mode determined by point counting and converted to mole per cent to calculate a model rock composition (see Wei *et al.*, 2009). Ferric content was fixed at a low value ($FeO:FeO_{3/2}$ = 20:1) reflecting the occurrence of graphite. A further simplification employed in the discussion below is to assume that, on the basis of equivalent mineral assemblage and similar modal data, the bulk rock composition of sample 0708b from Bahía Pia is broadly equivalent to that of sample 0703 from Ventisquero Roncagli. Difficulties related to site access meant it was impossible to return large samples for XRF analysis from most locations.

Figure 10a shows the equilibria modelled for 550–700 °C and 5–12.5 kbar, prepared with quartz in excess. As it is difficult to estimate the amount of H_2O present for temperature conditions above the water-saturated solidus, the method of White *et al.* (2001) was used, and these equilibria were calculated with fixed water content at a value that reflects the highest pressure sub-solidus assemblage. Most equilibria are tri or quadrivariant, with two divariant equilibria: one narrow, curved field involving the main S2 paragenesis of biotite, garnet, kyanite, staurolite, muscovite, plagioclase, quartz, rutile and ilmenite, and another at higher temperature involving biotite, garnet, kyanite, muscovite, quartz, plagioclase, rutile, ilmenite and liquid. The diagram has epidote-bearing equilibria at high-*P* and low-*T*, and staurolite-bearing equilibria restricted to 550–630 °C and < 9.3 kbar, outlined by a green line. Garnet-bearing assemblages occur at high-*P–T* conditions with a complex lower limit marked by a red line (Fig. 10a). Isopleths of garnet mode for relevant fields are shown (as percentages) in Fig. 10a, and $x(grt) = Fe/(Fe + Mg)$ and $z(grt) = Ca/$

Fig. 4. (a) Garnet with S1 inclusion trails and complex internal structures, including patchy turbid areas. Staurolite contains S2 inclusion trails that parallel the penetrative matrix foliation. Sample 0708, base of image 25 mm. (b) Simply twinned staurolite overgrowing folded S1 defined by biotite, muscovite, plagioclase, quartz and ilmenite. Sample 0501a, base of image 3.5 mm. (c) S2 staurolite, kyanite and garnet in mica schist from Ventisquero Roncagli area, partially retrogressed to randomly oriented muscovite and biotite. Sample 0703, base of image 3.5 mm. (d) Snowball inclusion trail texture in garnet core defined mostly by S1 quartz inclusion trails, enclosed in an inclusion-poor rim. Sample 0513, base of image 1.5 mm. (e) Complex structure in patchily recrystallized garnet. Turbid areas are inferred to be later than the clear area at the top of the grain, and, on the basis of microstructures inferred to have formed contemporary with the development of post-S1 growth of kyanite and staurolite. Sample 0708, base of image 1.5 mm. (f) Garnet with inclusions trails from a metamorphosed mafic dyke. Matrix hornblende defines S2 Sample 0501b, base of image 3.5 mm. (g) Sillimanite, biotite, garnet and plagioclase in a deformed migmatite from the contact aureole of a Beagle Suite granite intrusion. Garnet lacks the patchy recrystallization textures evident in samples from outside the aureoles. Sample 0510, base of image 3.5 mm.
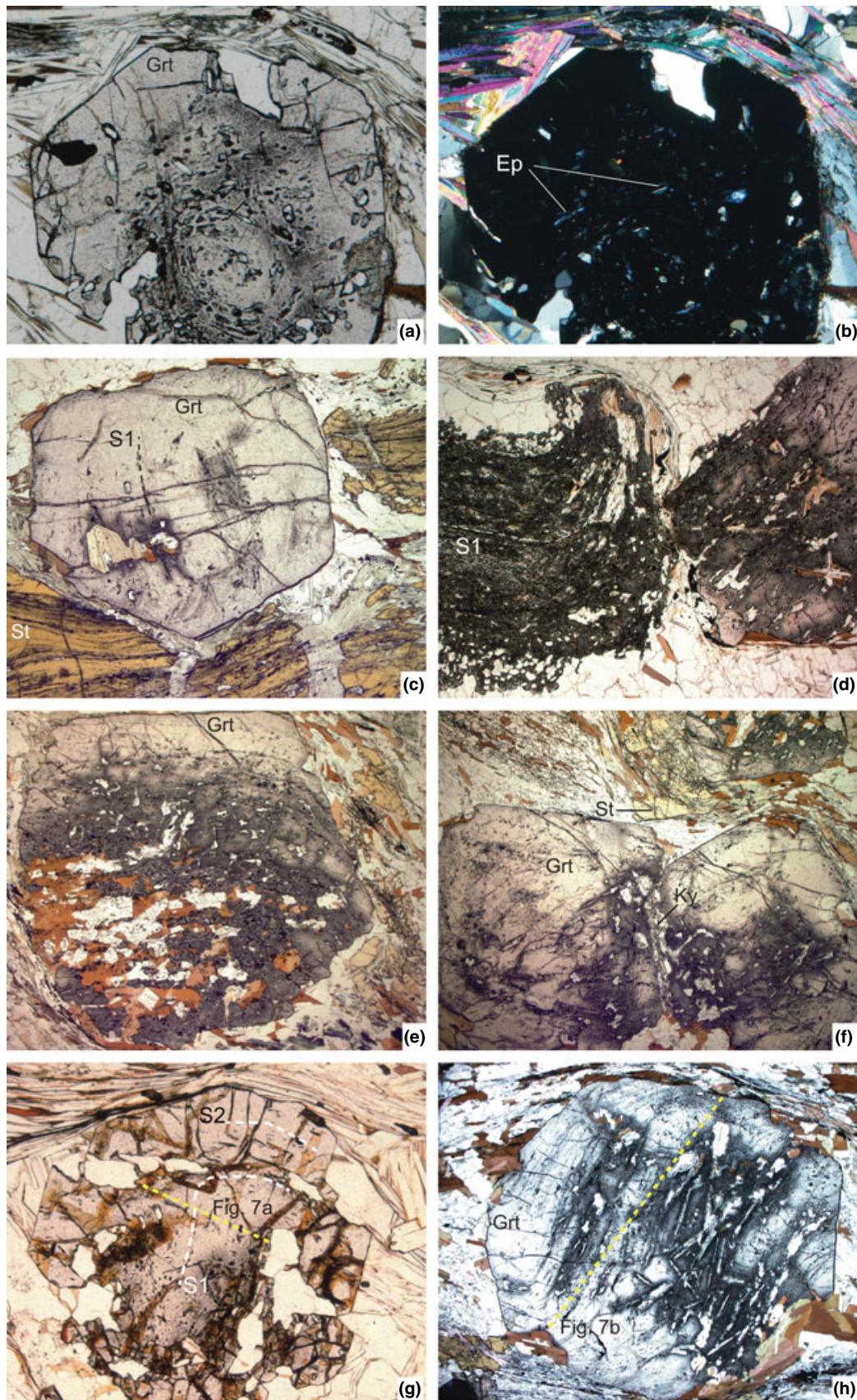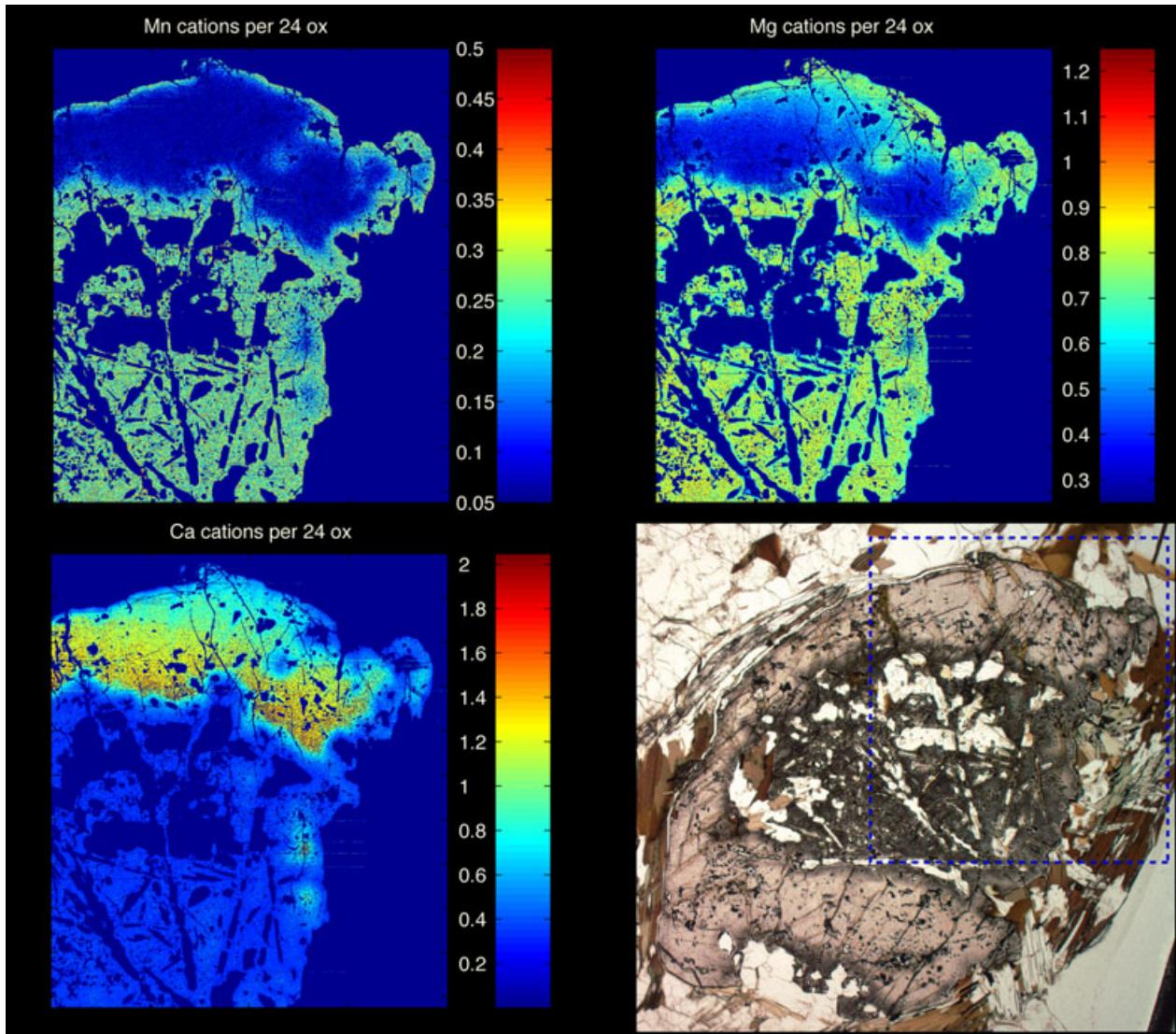
Fig. 6. Maps of Mn, Mg and Ca cations per 24 oxygen over part of a patchily recrystallized garnet grain involving a mantle of clear grossular-rich garnet and a core of turbid pyrope–spessartine-rich garnet intergrown with randomly oriented mica, plagioclase and quartz. Maps of X-ray intensity were collected using the University of NSW Cameca SX-50 microprobe, with matrix correction and image enhancement procedures following Clarke *et al.* (2001).

(Ca + Fe + Mg) contents in Fig. 10b,c, respectively. The main S2 assemblages reflect a restricted $P–T$ domain near $P \approx 9$ kbar and $T \approx 640$ °C where garnet and staurolite-bearing equilibria overlap (in the kyanite field). The narrowness of this divariant field reflects the near co-linearity of garnet and staurolite

Fig. 5. (a,b) Garnet core S1 epidote inclusion trails, enclosed in a comparatively inclusion-poor rim. Sample 0706B, Roncagli area, base of image 3 mm. (c) Garnet with a large biotite inclusion surrounded by turbid garnet (dark areas), and an isolated patch of turbid garnet apparently developed unrelated to the grain boundary. Adjacent staurolite has an intense S2 foliation defined mostly by ilmenite, which is oblique to weak S1 inclusion trails in garnet. Sample 0708, base of image 3.5 mm. (d) Contrasting textures in two adjacent garnet porphyroblasts. The left-hand porphyroblast preserves curved S1 inclusions trails defined by quartz, plagioclase, biotite and muscovite, whereas the right-hand porphyroblast has straight S1 inclusion trails truncated by turbid garnet patches that include large randomly oriented grains of biotite and muscovite. Sample 0501a, base of image 5 mm. (e) Clear garnet with fine-grained S1 inclusion trails (running across the top of the grain) mostly recrystallized to turbid garnet, biotite and plagioclase. Staurolite is adjacent to the upper right-hand side of garnet. Sample 0708, base of image 3.5 mm. (f) Two clear garnet grains with turbid areas and kyanite developed at their mutual boundary. S2 staurolite, biotite, plagioclase and quartz occur in the matrix. Sample 0708, base of image 3.5 mm. (g) Garnet with curved S1 inclusion trails, mostly defined by quartz and ilmenite. Grain has pronounced chemical zoning as shown the compositional profile collected oblique to the S1 inclusion trail along the dashed yellow line in Fig. 6a. Sample 0703, base of image 1 mm. (h) Garnet with turbid patches developed both at the grain edge and internally. Large random muscovite, biotite and plagioclase intergrown with turbid garnet truncate S1 inclusion trails in clear areas. Sample 0708, base of image 5 mm.

Table 2. Summary of EMP mineral chemistry data for metapelitic samples from Cordillera Darwin.

Sample	Garnet				Garnet				Biotite		Muscovite		Pl		St	Ep	Chl	Hbl
	Core				Rim				In Grt	S2	In Grt	S2	In Grt	S2	S2	In Grt	Post-S2	S2
	Alm	Sps	Prp	Grs	Alm	Sps	Prp	Grs	X_{Mg}	X_{Mg}	Si pfu	Si pfu	An	An	X_{Mg}	Czo	X_{Mg}	X_{Mg}
Pia1a																		
Grt–St–Bt	0.77	–	0.01	0.13	0.81	–	0.12	0.07	0.46			6.1	0.55	0.73	0.16			
Pia1b																		
Grt–Hbl					0.64	–	0.06	0.30						0.13				0.38
Pia2c																		
Grt–Sil–Bt					0.78	0.06	0.10	0.05		0.45		6.0		0.63				
Pia5b																		
Grt–St–Bt	0.71	0.08	0.12	0.11	0.69	0.14	0.14	0.06		0.29		5.3	0.25	0.50	0.20		0.59	
Pia 7c																		
Grt–St–Bt					0.75	0.06	0.12	0.04	0.45	0.48	6.0	6.0	0.72	0.81	0.27		0.41	
Pia 6a																		
Grt–Ky–St–Bt	0.68	0.03	0.04	0.18	0.79	0.05	0.10	0.04		0.46		6.0	0.25	0.26	0.10		0.25	
Pia 7c																		
Grt–St–Bt	0.71	0.02	0.10	0.06	0.75	0.06	0.12	0.03	0.41	0.45	6.0	6.0		0.38	0.18			
0703																		
Grt–Ky–St–Bt	0.69	0.04	0.14	0.12	0.54	0.12	0.05	0.25		0.43				0.26	0.16	0.56	0.54	
0708																		
Grt–Ky–St–Bt	0.61	0.14	0.05	0.25	0.74	0.07	0.12	0.08	0.52	0.52	6.2	6.3	0.35	0.74	0.24			

with respect to kyanite in terms of $X_{Fe} = Fe/(Fe + Mg)$ composition.

Conditions of $P \approx 12$ kbar and $T \approx 620$ °C can be recovered for S1 inclusion assemblages involving biotite, epidote, muscovite, albite-rich plagioclase and rutile, together with the composition of the garnet core [x(grt) $= Fe/(Fe + Mg) = 92$ and z(grt) $= Ca/(Ca + Fe + Mg) = 30$] in sample 0703 from Ventisquero Roncagli (red dot labelled 1 in Fig. 10a). This core composition is inferred to reflect the earliest stage of garnet growth, as patch textures associated with the development of S2 were not observed in garnet from Ventisquero Roncagli; were MnO to be considered in the model system subtly lower temperature conditions would probably be inferred. The pronounced chemical zoning of garnet from this sample from a grossular-rich core to an almandine–pyrope-rich rim (Fig. 7a) that is inferred to be contemporary with S2 staurolite and kyanite can be modelled as reflecting decompression from ~12 to 9 kbar through the quadrivariant field involving biotite, epidote, garnet, muscovite, plagioclase and rutile, and the trivariant field involving biotite, epidote, garnet, muscovite, plagioclase, rutile and ilmenite. Garnet mode is modelled as initially increasing on a prograde path; the composition of the intermediate mantle of garnet in this sample can be modelled as reflecting $P \approx 10.7$ kbar and $T \approx 630$ °C (red dot labelled as 2, Fig. 10a). The composition of the garnet rim [x(grt) $= 84$, z(grt) $= 13$] overlaps with the narrow divariant field involving the S2 paragenesis of biotite, garnet, kyanite, staurolite, muscovite, plagioclase, quartz, rutile and ilmenite, at $P \approx 9$ kbar and $T \approx 625$ °C. Garnet growth in this sample can thus be modelled via a P–T path dominated by decompression from 12 to 9 kbar, over 610–630 °C. Temperature conditions inferred for the garnet rim composition are slightly (5–10 °C) lower, but within error of the peak, inferred to have accompanied the formation of garnet

mantle compositions (red dot 2, Fig. 10a). Lower temperature conditions for garnet cores would be recovered in a model system involving MnO (Wei *et al*., 2009).

The complex garnet textures in sample 0708 from Bahía Pia can be modelled using a similar, more restricted P–T path than that inferred for the Ventisquero Roncagli sample. This restriction might reflect a sampling bias in the core analyses used, possibly related to partial grain recrystallization, along-strike variation in pressure conditions in Cordillera Darwin (Fig. 2), or errors associated with the bulk rock calculations. Taking the most calcic part of the clear garnet domains [x(grt) $= 9$, z(grt) $= 24$] as reflecting the earliest garnet growth, conditions for the quadrivariant S1 assemblage biotite, epidote, garnet, muscovite, plagioclase, and rutile involved $P \approx 10.5$ kbar and $T \approx 610$ °C (marked by white dot labelled 1, Fig. 10a). There are no epidote inclusions in garnet from sample 0708, but epidote does occur as inclusions in metapelitic garnet elsewhere in Bahía Pia. Garnet mode is again modelled as coupled with increasing temperature conditions, possibly up to 5% in the trivariant field involving biotite, epidote, garnet, muscovite, plagioclase, quartz, rutile and ilmenite. The composition of the garnet rim, and turbid parts of garnet from this rock [x(grt) $= 84$, z(grt) $= 13$] is modelled as falling at $P \approx 8.8$ kbar and $T \approx 620$ °C in the low-P part of the trivariant field involving biotite, garnet, staurolite, muscovite, plagioclase, quartz, rutile and ilmenite, shown by the white dot labelled 2 (Fig. 10a). This lies just outside the divariant field reflecting the main S2 paragenesis, but probably within error when issues related to the method of whole-rock calculation are considered. A decompressional path extending below the divariant field involving biotite, garnet, kyanite, staurolite, muscovite, plagioclase, quartz, rutile and ilmenite, is inferred to have resulted
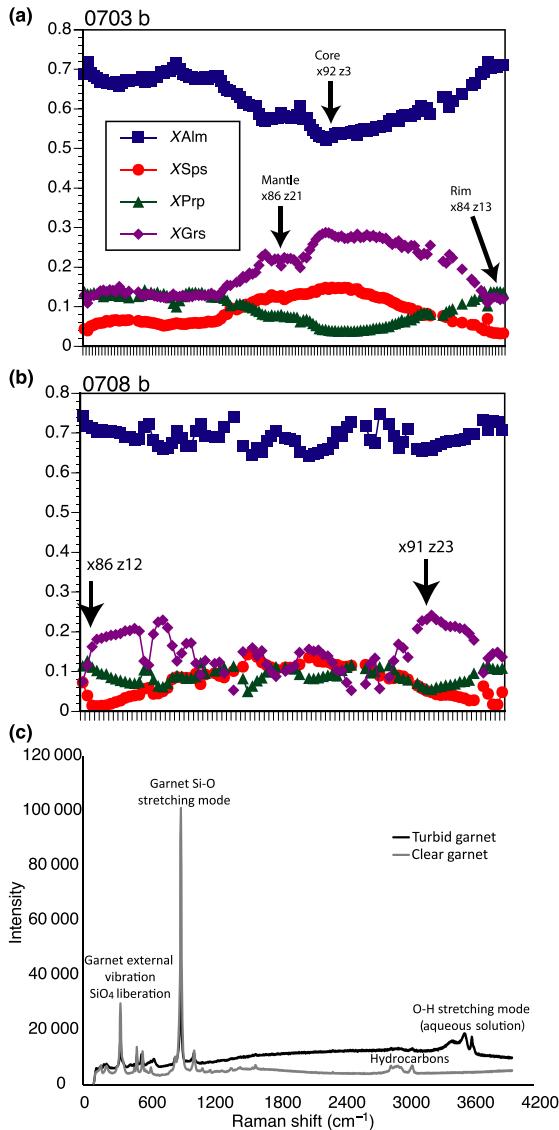
Fig. 7. (a) Traverse through garnet grain from sample 0703 from Ventisquero Roncagli, showing variation in X_{alm} = Fe/(Fe + Mn + Mg + Ca), X_{spess} = Mn/(Fe + Mn + Mg + Ca), X_{py} = Mg/(Fe + Mn + Mg + Ca) and X_{gross} = Ca/(Fe + Mn + Mg + Ca). X_{Fe} = Fe/(Fe + Mg) and zCa = Ca/(Fe + Mg + Ca) values corresponding to isopleth values modelled in THERMOCALC are shown for parts of the grain core, mantle and rim. All analyses of mineral inclusions were removed from the profile. (b) Traverse through a garnet grain in sample 0708, with irregularly developed turbid patches. All variables as given for this figure. Though a bell-shaped pattern is still defined by spessartine content, equivalent trends in almandine, pyrope and grossular contents are highly disrupted in areas corresponding to the turbid garnet. (c) Raman spectra from a garnet from sample Pia7C/1 from clear and turbid areas within the garnet.

in a substantial decrease in garnet mode from a maximum of ~5% to <1% garnet. This predicted change provides a plausible mechanism for the development of the patchy turbid textures, as discussed below. Substantial errors (1–3 kbar) could be expected for all the

absolute pressure conditions inferred above, related to analytical errors and the means by which a whole-rock composition was established. Nonetheless, the *relative* pressure change between conditions inferred for the inclusion and matrix assemblage could be expected to be more robust (e.g. Worley & Powell, 2000).

The presence of sillimanite in contact aureoles around Beagle Suite plutons at various locations in Bahía Pia and Seno Romanche reflects exhumation and localized heating from the kyanite field to sillimanite field. Migmatitic assemblages at sample site 0510 involving sillimanite, plagioclase, biotite and ilmenite, with or without garnet (Fig. 4g), reflect $T \approx 690\ °C$ at $P \approx 6$ kbar (Fig. 10). These sillimanite assemblages are not widespread (cf. Kohn *et al.*, 1993). Post-S2 chlorite reflects retrogression at low-grade conditions, as reflected by the small chlorite-bearing fields at the low-P–T extent of Fig. 10a.

DISCUSSION

Patchy recrystallization of garnet

The honeycomb and patch textures (Figs 4a & 5h) of turbid, spessartine–pyrope-rich garnet in the Bahía Pia samples might be interpreted as early formed garnet, overgrown by later grossular-rich garnet. However, several features counter this interpretation. The 'atoll'-like textures are always incomplete, the minerals intergrown with turbid garnet are commonly randomly oriented, and one to two orders of magnitude larger than S1 inclusions. The minerals intergrown with turbid garnet do not define S1, but may cut S1 and be continuous with minerals defining S2 in the surrounding quartz–mica-rich matrix (Fig. 5e). Mineral intergrowths with turbid garnet are comparable in grain size to matrix S2 minerals. They are also generally the same minerals, being dominated by quartz and mica. In detail, turbid, spessartine–pyrope-rich garnet also encloses grossular-rich garnet (Fig. 6) and its development seems enhanced near sites of staurolite and kyanite growth (Fig. 5e,f). Accepting that turbid, spessartine–pyrope-rich garnet formed later than the grossular-rich garnet begs an interpretation for a mechanism responsible for garnet recrystallization decoupled from the grain margin, that is, one apparently less affected by kinetic aspects influencing diffusion.

Turbid garnet from Bahía Pia (Fig. 5c,e) texturally resembles chemically homogeneous 'honeycomb' garnet in high-pressure rocks from the Tauern Window of the Eastern Alps, interpreted to result from precipitation from a wetting fluid along quartz-quartz grain boundaries (Hawkins *et al.*, 2007). Minerals intergrown with the turbid garnet from Bahía Pia are dominated by muscovite and biotite, abundant quartz and, apparently, reflect a process coupled with reduced garnet mode. Turbid garnet regions also have a similar appearance to cloudy garnet observed in the Acadian
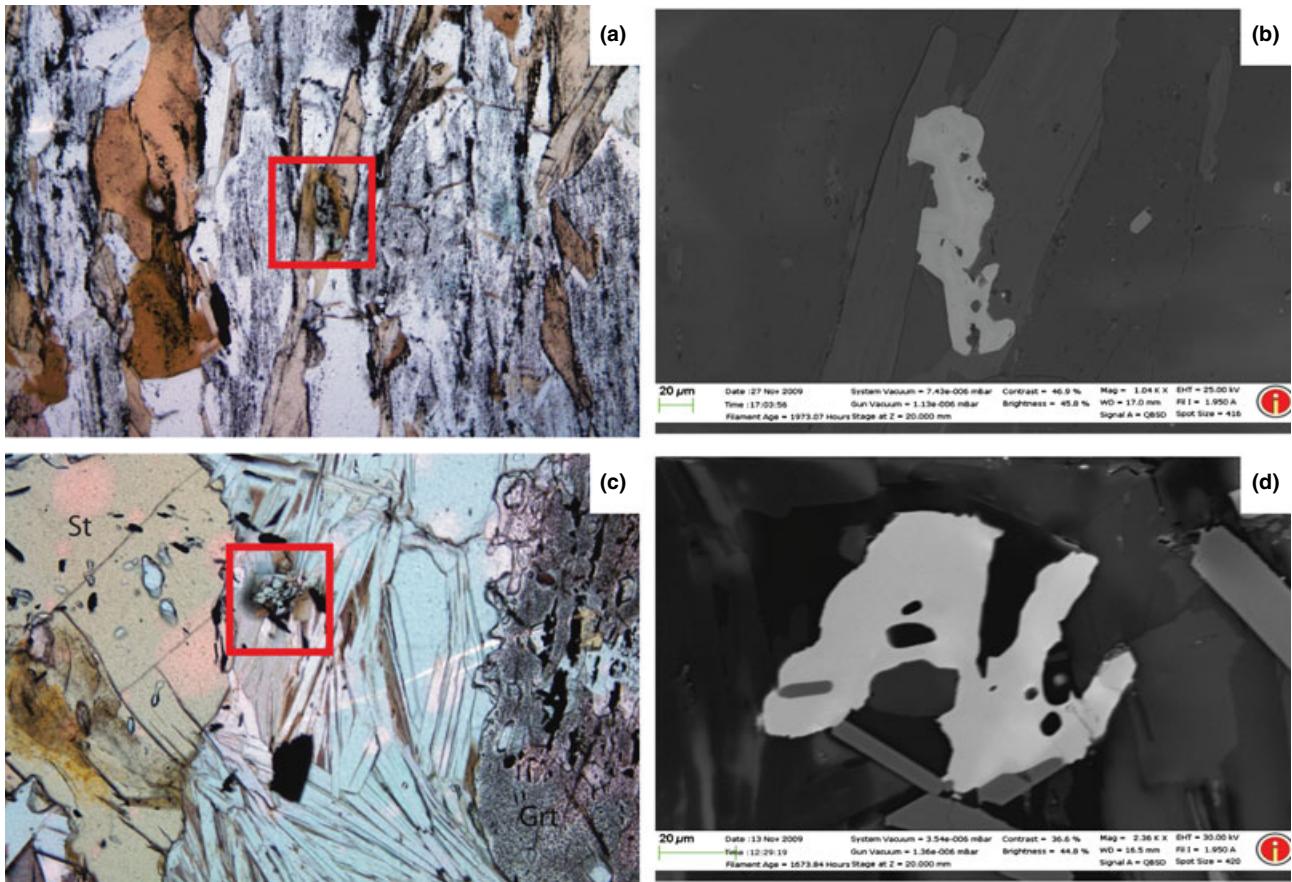
Fig. 8. (a) Monazite grain with visible pleochroic halo from grain mount Z5490 prepared from sample 0708a. Square indicates monazite. Monazite occurs in S2 biotite. Base of image is 1.5 mm. (b) Backscattered electron (BSE) image of monazite in (a); there is minimal zoning. (c) Monazite grain with visible pleochroic halo from grain mount Z5495 prepared from sample 0501. Monazite occurs in S2 defined by intergrown muscovite and staurolite (left). Turbid garnet is visible on the right of the image. Base of image is 1.5 mm. (d) BSE image of monazite in (c); there is minimal zoning.

zone of western New England, north-eastern United States of America, interpreted to be the result of 1–2 μm fluid and mineral inclusions developed during fluid assisted metasomatism along grain boundaries and cracks (Hames & Menard, 1993; Whitney *et al.*, 1996a,b). Fluid ingress late in the development of S2, possibly coupled with the fracturing and site-specific partial recrystallization of garnet (Whitney, 1991), can also account, for example, from Bahía Pia.

Evidence for the presence of fluid within turbid garnet was found during Raman spectroscopy, indicating the presence of an aqueous saline solution (Fig. 7c). Fluid could have been sourced from underthrust sheets of Rocas Verdes metasedimentary rocks experiencing contemporary prograde metamorphism. Hydro-fracturing could have then exposed parts of earlier-formed grain cores of compositions formed at higher pressure and lower temperature (e.g. Carlson & Gordon, 2004) and enhanced reaction coupled with staurolite and kyanite growth. Reduced garnet mode, interpreted as related to terrane-wide uplift, can explain the higher spessartine content in the turbid garnet whereby reduced modes of secondary garnet

resorbed all Mn from earlier-formed garnet. Large mica and plagioclase grains intergrown with the turbid garnet, and large staurolite and kyanite adjacent to garnet, would probably require that intergranular diffusion occurred on a scale at least as large as the garnet porphyroblasts (e.g. Carmichael, 1969). The lack of the development of turbid garnet in the Ventisquero Roncagli examples most probably reflects lower fluid-rock ratios in those rocks, possibly related to them being more distant to areas of Rocas Verdes rocks undergoing prograde metamorphism.

A model for metamorphism driven by back-arc basin closure

The southern sector of the Rocas Verdes basin generally is interpreted to have been wider and undergone greater subsidence than northern parts of the basin (Dalziel & Elliot, 1971; Dott *et al.*, 1982; Wilson, 1991; Olivero & Martinioni, 2001; Fig. 11a). This interpretation focuses attention on the need for a mechanism that accounts for the fate of a larger area of mafic ocean floor to the southern part of the basin (Fig. 11a).

Table 3. Summary of SHRIMP U–Pb data for monazite grains from Cordillera Darwin.

Grain. spot	U (ppm)	Th (ppm)	Th/U	^{206}Pb* (ppm)	^{204}Pb/^{206}Pb	f$_{206}$%	Total				Radiogenic		Age (Ma)	
							^{238}U/^{206}Pb	±	^{207}Pb/^{206}Pb	±	^{206}Pb/^{238}U	±	^{206}Pb/^{238}U	±
Z5495														
4	3045	17 975	5.90	29.1	0.000888	0.79	89.93	1.03	0.0537	0.0006	0.0110	0.0001	70.7	0.8
5.1	3500	19 570	5.59	33.8	0.000729	0.87	88.93	1.04	0.0544	0.0007	0.0111	0.0001	71.5	0.8
5.2	4038	23 226	5.75	45.3	0.004155	7.34	76.57	1.30	0.1058	0.0035	0.0121	0.0002		
6	3540	22 147	6.26	34.4	0.000754	0.47	88.44	1.18	0.0512	0.0006	0.0113	0.0002	72.1	1.0
7	4518	25 456	5.63	45.2	0.000357	0.46	85.94	1.02	0.0511	0.0007	0.0116	0.0001	74.2	0.9
9	3072	8876	2.89	30.9	0.000464	0.36	85.44	0.93	0.0504	0.0006	0.0117	0.0001	74.7	0.8
10	3811	17 501	4.59	39.5	0.003030	5.20	82.81	0.89	0.0887	0.0017	0.0114	0.0001	73.4	0.8
8	3044	10 700	3.52	30.6	0.000377	0.33	85.40	0.93	0.0501	0.0007	0.0117	0.0001	74.8	0.8
2	3098	12 341	3.98	31.1	0.000281	0.23	85.46	0.94	0.0493	0.0006	0.0117	0.0001	74.8	0.8
1	3194	13 865	4.34	32.2	0.000629	0.41	85.19	0.93	0.0508	0.0010	0.0117	0.0001	74.9	0.8
3	3061	18 879	6.17	29.8	0.000376	0.38	88.20	0.97	0.0504	0.0007	0.0113	0.0001	72.4	0.8
Z5490														
7	4521	19 885	4.40	45.5	0.000734	0.92	85.34	0.94	0.0548	0.0006	0.0116	0.0001	74.4	0.8
8	4915	44 461	9.05	47.6	0.000846	0.64	88.64	0.95	0.0525	0.0005	0.0112	0.0001	71.9	0.8
9	3358	18 278	5.44	32.5	0.000520	0.36	88.72	0.97	0.0503	0.0006	0.0112	0.0001	72.0	0.8
10	3530	17 448	4.94	34.1	0.000472	0.47	88.92	0.97	0.0512	0.0006	0.0112	0.0001	71.8	0.8
12	4214	27 185	6.45	42.6	0.001763	3.07	84.96	0.91	0.0718	0.0006	0.0114	0.0001	73.1	0.8
11	4167	18 095	4.34	41.9	0.001934	3.84	85.36	0.92	0.0779	0.0018	0.0113	0.0001	72.2	0.8
14	4074	28 099	6.90	39.5	0.000268	0.44	88.69	0.95	0.0509	0.0007	0.0112	0.0001	72.0	0.8
15	3657	23 703	6.48	36.3	0.000267	0.52	86.48	0.94	0.0516	0.0006	0.0115	0.0001	73.7	0.8
13	3695	22 416	6.07	36.2	0.000954	1.53	87.69	0.95	0.0596	0.0008	0.0112	0.0001	72.0	0.8
4	3838	20 962	5.46	36.3	0.000266	0.33	90.72	0.98	0.0500	0.0006	0.0110	0.0001	70.4	0.8
3	3860	42 263	10.95	36.7	0.000565	0.73	90.41	0.98	0.0532	0.0011	0.0110	0.0001	70.4	0.8
2	4284	23 300	5.44	41.4	0.000393	0.57	88.96	0.96	0.0519	0.0005	0.0112	0.0001	71.6	0.8
5	4549	20 918	4.60	45.2	0.001084	1.86	86.38	0.93	0.0622	0.0009	0.0114	0.0001	72.8	0.8
Z5491														
11.2	3719	21 484	5.78	37.0	0.000878	2.04	86.33	0.93	0.0637	0.0011	0.0113	0.0001	72.7	0.8
3	4080	19 263	4.72	41.3	0.000124	0.53	84.93	0.93	0.0517	0.0006	0.0117	0.0001	75.1	0.8
4	3825	21 630	5.66	37.6	–	0.38	87.45	0.96	0.0505	0.0006	0.0114	0.0001	73.0	0.8
2	3640	18 820	5.17	36.3	0.000174	0.44	86.23	0.94	0.0510	0.0009	0.0115	0.0001	74.0	0.8
5	3618	20 838	5.76	35.7	0.000460	1.27	87.16	0.95	0.0576	0.0006	0.0113	0.0001	72.6	0.8
1	4435	28 392	6.40	42.7	0.000267	0.80	89.21	0.97	0.0538	0.0006	0.0111	0.0001	71.3	0.8
6	4465	43 131	9.66	43.5	0.000000	0.27	88.20	0.95	0.0496	0.0007	0.0113	0.0001	72.5	0.8
7	3752	21 150	5.64	36.8	0.000152	0.41	87.64	0.96	0.0507	0.0006	0.0114	0.0001	72.8	0.8
8	4087	23 707	5.80	40.0	0.000121	0.34	87.71	0.96	0.0502	0.0007	0.0114	0.0001	72.8	0.8
9	3980	34 858	8.76	38.3	0.000107	0.69	89.16	0.97	0.0529	0.0006	0.0111	0.0001	71.4	0.8
12	5778	42 830	7.41	56.5	0.000012	0.61	87.91	0.96	0.0523	0.0006	0.0113	0.0001	72.5	0.8
11.1	7558	77 235	10.22	71.5	0.000061	0.99	90.80	0.98	0.0552	0.0006	0.0109	0.0001	69.9	0.8
10	14247	166 607	11.69	143	0.000092	2.19	85.73	0.93	0.0649	0.0007	0.0114	0.0001	73.1	0.8

	Age	± no std		± include std	
wtd ave most	72.61	0.46	1.55	1.13	36 of 37 analyses, MSWD = 2.9
wtd ave Z5490	71.97	0.61	1.05	0.76	12 of 13 analyses, MSWD = 1.5
wtd ave Z5491	72.60	0.47	0.79	0.57	11 of 13 analyses, MSWD = 0.92

Uncertainties given at the one sigma level; the error in the 44069 reference monazite calibration was 1.19%, 0.62% and 0.45% for the analytical sessions; f206% denotes the percentage of ^{206}Pb that is common Pb; and the correction for common Pb for the U/Pb data has been made using the measured ^{238}U/^{206}Pb and ^{207}Pb/^{206}Pb ratios following Tera & Wasserburg (1972) as outlined in Williams (1998).

This issue, and the burial of continental crust to ~40 km as a consequence of tectonic under-thrusting during back-arc basin closure can be explained by a thickening of continental crust following incipient subduction of the back arc basin's mafic floor (Fig. 11b). The following discussion draws on regional relationships and geochronology (Table 1) to evaluate tectonic models for the history of Cordillera Darwin schists. The combined effects of tectonic imbrication and further subduction appear to have juxtaposed continental crust of the Gondwana margin and the volcanic arc, in relative positions close to where they are currently.

Attempted subduction and thickening of the leading edge of the continental margin under the volcanic arc (Fig. 11c) accounts for the prograde S1 assemblages now preserved as S1 inclusion trails in garnet from Cordillera Darwin. This tectonic loading on the leading edge of the continent was accompanied by the development of the flexural Magallanes foreland basin (Natland *et al.*, 1974; Biddle *et al.*, 1986; Wilson, 1991). Foreland basin sedimentation had begun by *c.* 92 Ma in northern Patagonia (Fildani *et al.*, 2003) and possibly slightly later in Tierra del Fuego (McAtamney *et al.*, 2009). Cross-cutting relationships between plutons of the Beagle Suite at Seno Ventisquero indicate that continental underthrusting and then initial obduction occurred prior to *c.* 86 Ma, while subduction continued along the proto-Pacific margin (Klepeis *et al.*, 2010). Relative mantle and continental crustal
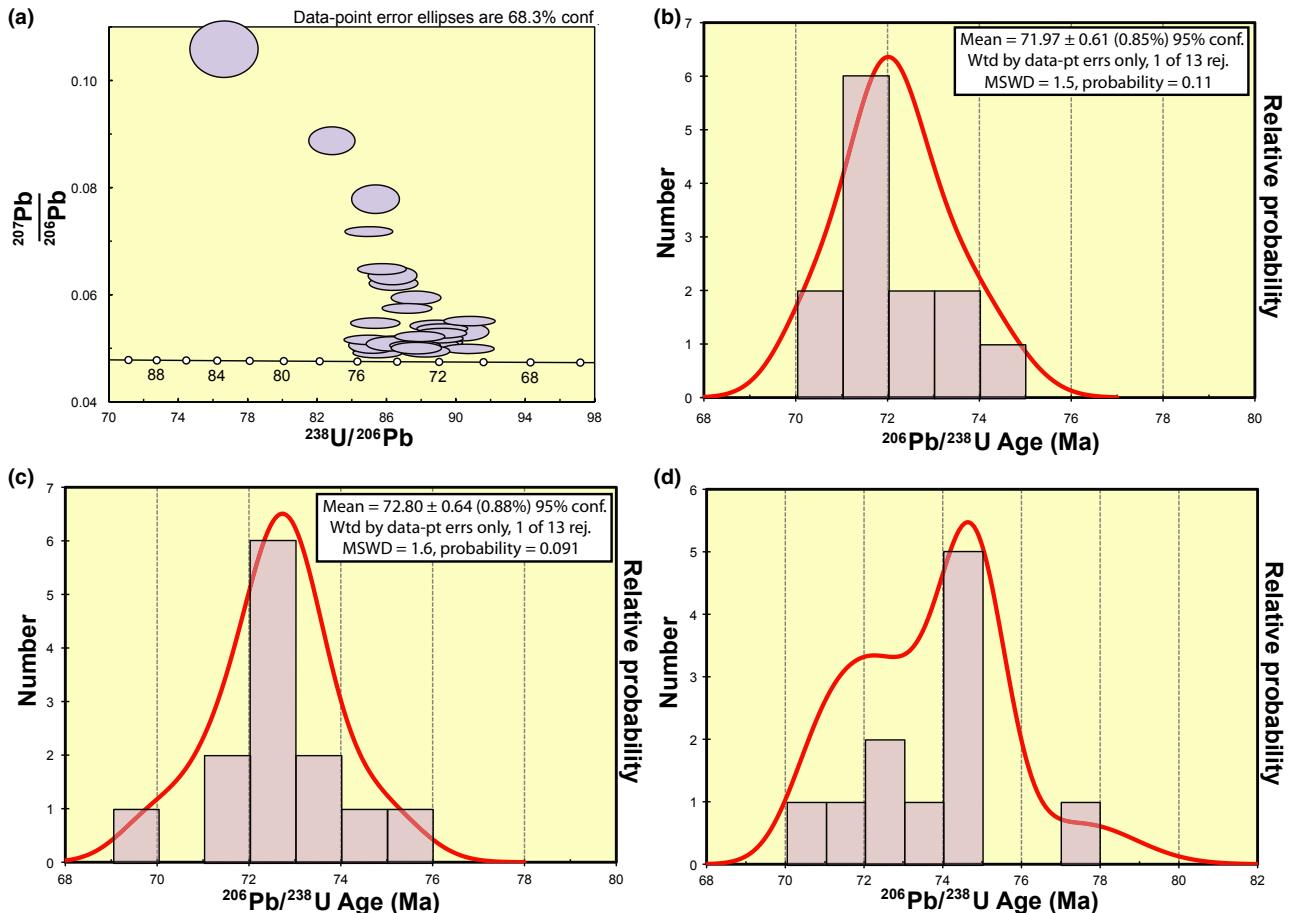
Fig. 9. (a) Tera-Wasserburg diagram showing $^{207}Pb/^{206}Pb$ *v.* $^{238}U/^{206}Pb$ ratios for monazite analyses collected from all three grains mounts. Error ellipses are shown at 68.3% confidence. (b) Histogram of ages from grain mount Z5490, sample 0708. (c) Histogram of ages from grain mount Z5491, sample 0708. (d) Histogram of ages from grain mount Z5495, sample 0501. Due to limited data and scatter a meaningful age for this mount was not found, however, results are consistent with the other two mounts.

buoyancy could have limited the descent of the Gondwana margin (e.g. Aitchison *et al.*, 1995; Harris *et al.*, 2000).

Monazite in the Bahía Pia schists most probably formed from the partial breakdown of xenotime. As it only occurs in micaceous S2 assemblages that include staurolite and kyanite, the 72.6 ± 1.1 Ma monazite age is inferred to reflect a stage of the terrane's exhumation (Figs 10 & 11d). High-grade rocks in Bahía Pia thus underwent nearly isothermal decompression to form staurolite-kyanite-bearing assemblages at $P \approx 9$ kbar by *c.* 73 Ma, and migmatitic sillimanite assemblages at $P \approx 6$ kbar by *c.* 70 Ma (Fig. 11d; S. Thomson & K. A. Klepeis, unpublished U–Pb ages of Beagle suite plutons). These data are consistent with *c.* 70–69 Ma $^{40}Ar/^{39}Ar$ muscovite and biotite cooling ages, and *c.* 76–73 Ma hornblende ages obtained from high-grade rocks in Bahía Pia (Grunow *et al.*, 1992; Kohn *et al.*, 1995). Model closure temperatures for Ar retention in hornblende, muscovite and biotite, together with the $^{40}Ar/^{39}Ar$ ages were used by Kohn *et al.* (1995) to infer

that uplift and cooling of the high-grade rocks in Cordillera Darwin was initially comparatively rapid. Fission-track ages (Nelson, 1982; Gombosi *et al.*, 2009) record continued, somewhat slower, uplift of Cordillera Darwin into the Neogene. Termination of the Cretaceous metamorphism could have been ultimately controlled by oceanic slab break-off, and foundering of the leading Rocas Basin mafic floor (Fig. 11e). Continued crustal shortening during and after uplift of the high-grade rocks in Cordillera Darwin is evident in the development of basement-cored macroscopic folds and back thrusts, with the eastward propagation of contemporary thrust faults into the Magallanes foreland basin (Klepeis *et al.*, 2010; Fig. 11e).

Although there is a general consensus that high-grade metamorphism in Cordillera Darwin rocks was induced by tectonic burial of the Gondawana margin and quasi-oceanic crust associated with closure of the Rocas Verdes back-arc basin, alternative models for their exhumation also have been proposed. Dalziel & Brown (1989) inferred that the high-grade rocks
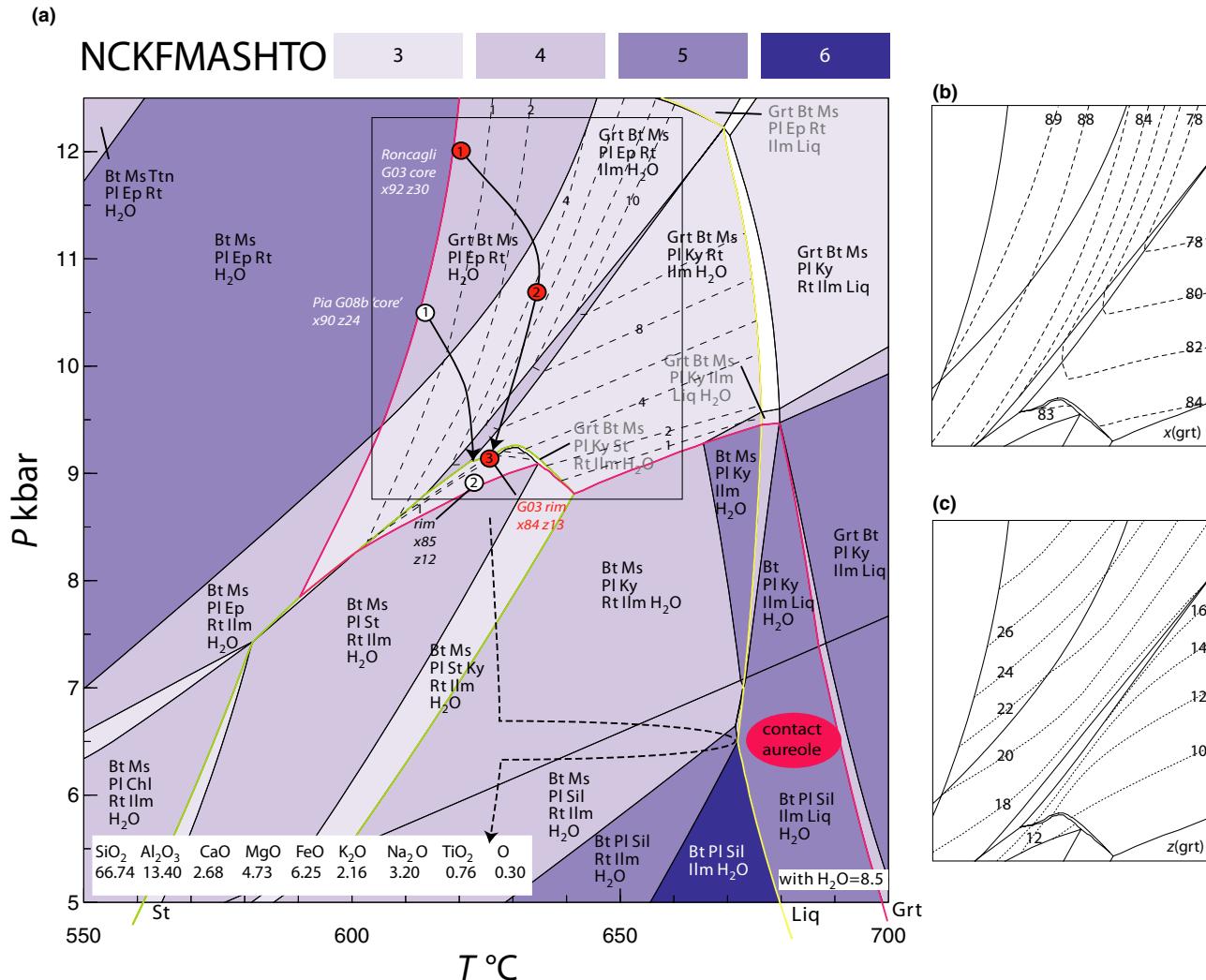
(a)

Fig. 10. (a) Calculated $Na_2O–CaO–K_2O–FeO–MgO–Al_2O_3–SiO_2–H_2O–TiO_2–Fe_2O_3$ (NCKFMASHTO) pseudosection indicating the position of mineral inclusion assemblages and inferred $P–T$ path followed by samples 0708 (White dots; Bahía Pia) and 0703 (Red dots; Roncagli). A representative whole-rock composition was calculated from modal data and representative microprobe analyses of S2 minerals and garnet rims. Garnet cores were excluded from the calculations in a manner following Marmo *et al.* (2002). Isopleths of garnet mode are shown for relevant fields. Green line indicates the boundaries of staurolite-bearing equilibria, red line indicates the lower pressure limit of garnet-bearing equilibria and the yellow line indicates the solidus. Contact aureole refers to sillimanite-bearing assemblages that surround plutons of the Beagle Suite grantoids. (b,c) Isopleths of $x(grt) = Fe/(Fe + Mg)$ and $z(grt) = Ca/(Ca + Fe + Mg)$ for garnet in relevant fields, used to locate the $P–T$ position of core and mantle inclusion assemblages for the two samples.

defined a metamorphic core complex, on the basis of similarities between Cordillera Darwin and the Shuswap metamorphic core complex in the North American Cordillera, where uplift and exhumation is inferred to have been driven by extension (Armstrong, 1982). However, the southern boundary of amphibolite facies rocks in Bahía Pia is a normal fault, which acts as a step-over between sinistral strike-slip faults (Figs 2a, d: Klepeis *et al.*, 2010), and the northern boundary is the Parry Thrust in Seno Parry (Klepeis *et al.*, 2010).

In an alternative model, Cunningham (1995) suggested that basement-involved shortening and the exhumation of high-grade rocks in Cordillera Darwin was controlled by transpression related to oblique-slip faulting observed along the Beagle Channel. This model requires an increase in metamorphic grade towards the channel, inferred as being present at Ventisquero Roncagli by Cunningham (1995), but lacking at Bahía Pia and elsewhere along the western reaches of the Beagle Channel. In addition, our observations at Ventisquero Roncagli suggest that variations in mineral assemblage in this region are mostly controlled by lithology, not grade. Greenschist facies rocks immediately north of the Beagle Channel (Fig. 2) in Bahía Pia indicate that metamorphic grade
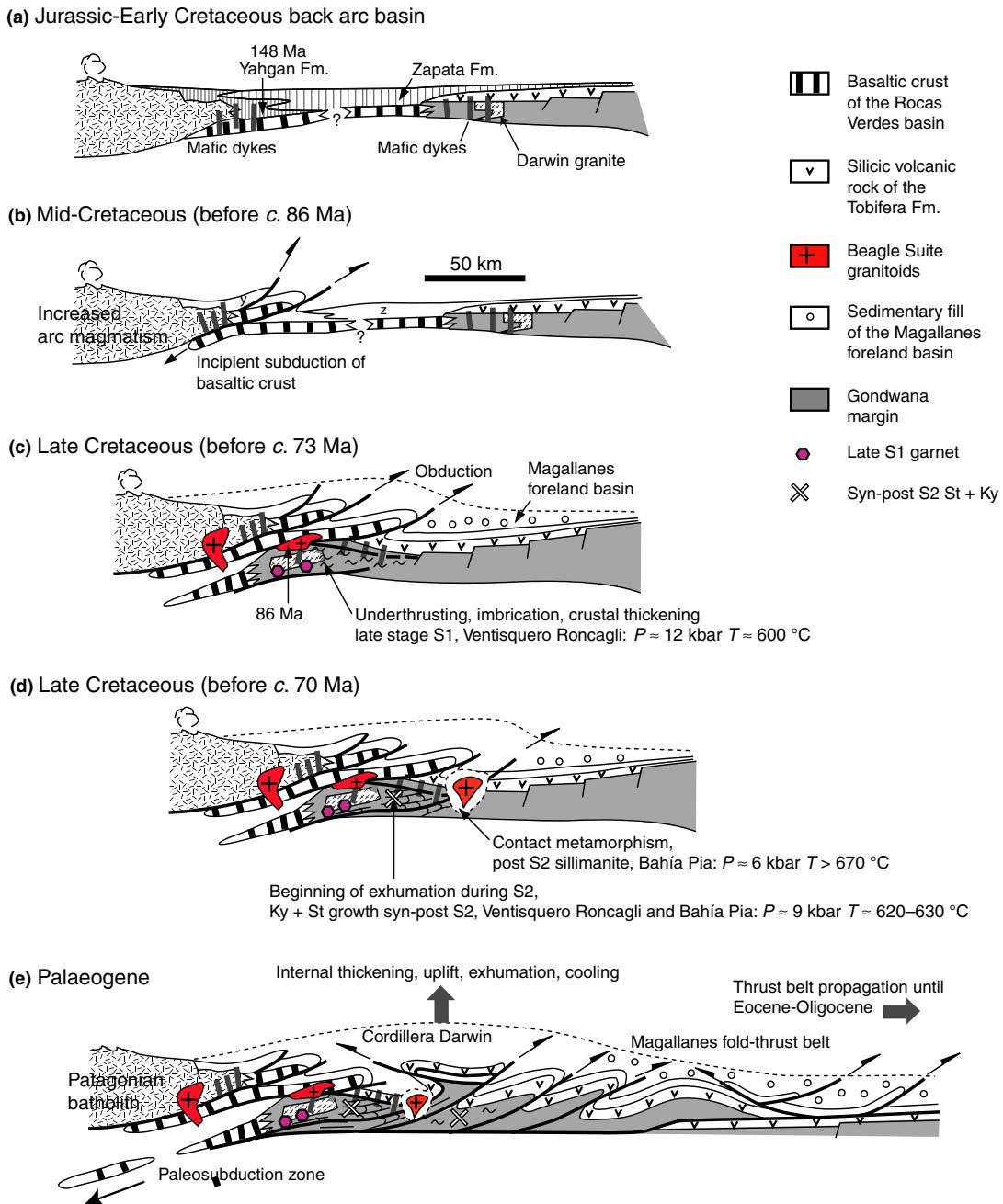
(a) Jurassic-Early Cretaceous back arc basin

(b) Mid-Cretaceous (before *c.* 86 Ma)

(c) Late Cretaceous (before *c.* 73 Ma)

(d) Late Cretaceous (before *c.* 70 Ma)

(e) Palaeogene

Fig. 11. Cartoon summarizing the Late Jurassic to Palaeogene evolution of Cordillera Darwin, the Rocas Verdes basin and the Magallanes foreland fold-thrust belt at the latitude of Tierra del Fuego. (a) Rifting, dyking and bimodal volcanism forms the quasi-oceanic Rocas Verdes rift basin by the Late Jurassic. Basin fill comprising the Zapata and Yahgan Formations thickens to the south, its width is uncertain, and arc magmatism was absent. (b) Compression initiated by *c.* 100 Ma led to subduction of the basaltic floor beneath the batholith to form a narrow thrust wedge comprised of mafic floor fragments and deformed volcanic and sedimentary basin fill. (c) Collision between the Patagonian batholith and South American continental crust resulted in continental crust and sequences of silicic volcanic rock (i.e. the Tobifera Formation) being underthrust beneath the batholith, contemporary with prograde S1 mineral inclusion trails in garnet that reflect *P* ≈ 12 kbar and *T* ≈ 600 °C in rocks at Bahía Pia and Ventisquero Roncagli. High-grade shear zones exposed at Bahías Pia and Parry cut all penetrative foliations and reflect tectonic uplift prior to *c.* 86 Ma, the age of the oldest Beagle suite granitoid in western Cordillera Darwin. Crustal loading and flexure created the Magallanes foreland basin. (d) Syn- to post-S2 kyanite–staurolite-bearing assemblages in parts of Cordillera Darwin now exposed between Bahía Pia and Ventisquero Roncagli reflect initial uplift to *P* ≈ 9 kbar by *c.* 73 Ma. Sillimanite-bearing migmatitic assemblages in contact aureoles to Beagle Suite plutons in Bahía Pia reflect further uplift to *P* ≈ 6 kbar by *c.* 70 Ma. (e) On-going collision between the Patagonian batholith and South American continental crust resulted in internal thickening, uplift and exhumation of hinterland thrusts in Cordillera Darwin. In response to this thickening of the internal part of the wedge, the Magallanes fold-thrust belt propagated into the foreland, deformation being over by the Eocene–Oligocene. Late Tertiary strike-slip faults omitted from the profiles for simplicity.

increases away from the channel, inconsistent with a model of exhumation having been driven by transpression along the Beagle Channel. In addition, all observed strike-slip faults cut F3 structures and all exhumation-related fabrics, indicating that they postdate the main phase of exhumation (Klepeis *et al.*, 2010). U–Pb zircon data indicate that most strike-slip and oblique-slip features formed after the Eocene (Gombosi *et al.*, 2009). The inverted northern metamorphic profile (Fig. 2d) and all other field relationships discussed in this paper are most consistent with exhumation having been synchronous with, and controlled by, thrusting.

ACKNOWLEDGEMENTS

REFERENCES

Aitchison, J.C., Clarke, G.L., Meffre, S. & Cluzel, D., 1995. Eocene arc-continent collision in New Caledonia and implications for regional southwest Pacific tectonic evolution. *Geology*, **23**, 161–164.

Alabaster, T. & Storey, B.C., 1990. Modified Gulf of California model for South Georgia, north Scotia Ridge, and implications for the Rocas Verdes back-arc basin, southern Andes. *Geology*, **18**, 497–500.

Aleinikoff, J., Schench, W., Plank, M. *et al.*, 2006. Deciphering igneous and metamorphic events in high-grade rocks of the Wilmington Complex, Delaware: morphology, cathodoluminescence and backscattered electron zoning, and SHRIMP U–Pb geochronology of zircon monazite. *Geological Society of America Bulletin*, **118**, 39–64.

Allen, R.B., 1982. Geología de la Cordillera Sarmiento, Andes Patagónicos, entre los 51°00′ y 52°15′ Lat. S, Magallanes, Chile. *Servicio Nacional de Geología y Minería Boletín, Santiago*, **38**, 46.

Alvarez-Marrón, J., McClay, K.R., Harambour, S., Rojas, L. & Skarmeta, J., 1993. Geometry and evolution of the frontal part of the Magallanes foreland thrust and fold belt (Vicuña Area), Tierra del Fuego, Southern Chile. *American Association of Petroleum Geologists Bulletin*, **77**, 1904–1921.

Armstrong, R.L., 1982. Cordilleran metamorphic core complexes – from Arizona to southern Canada. *Annual Review of Earth and Planetary Science*, **10**, 129–154.

Barbeau, D.L., Jr., Olivero, E.B., Swanson-Hysell, N.L., Zahid, K.M., Murray, K.E & Gehrels, G.E., 2009. Detrital-zircon geochronology of the eastern Magallanes foreland basin: implications for Eocene kinematics of the northern Scotia Arc and Drake Passage. *Earth and Planetary Science Letters*, **284**, 489–503.

Bersani, D., Andò, S., Vignola, P. *et al.*, 2009. Micro-Raman spectroscopy as a routine tool for garnet analysis. *Spectrochimica Acta Part A*, **73**, 484–491.

Biddle, K.T., Uliana, M.A., Mitchum, R.M., Fitzgerald, M.G. & Wright, R.C., 1986. The stratigraphic and structural evolution of the central and eastern Magallanes basin, southern South America. *Special Publication of the International Association of Sedimentologists*, **8**, 41–61.

Bruhn, R., Stern, C. & de Wit, M., 1978. Field and geochemical data bearing on the development of a Mesozoic volcano-tectonic rift zone and back-arc basin in southernmost South America. *Earth and Planetary Science Letters*, **41**, 32–46.

Bucher, K. & Frey, M., 1994. *Petrogenesis of Metamorphic Rocks*, 6th edn. Springer-Verlag Telos, Berlin, pp. 309–310.

Calderón, M., Fildani, A., Hervé, F., Fanning, C.M., Weislogel, A. & Cordani, U., 2007. Late Jurassic bimodal magmatism in the northern sea-floor remnant of the Rocas Verdes basin, southern Patagonian Andes. *Journal of the Geological Society*, **164**, 1011–1022.

Carlson, W.D. & Gordon, C.L., 2004. Effects of matrix grain size on the kinetics of intergranular diffusion. *Journal of Metamorphic Geology*, **22**, 733–742.

Carmichael, D.M., 1969. On the mechanism of prograde metamorphic reactions in quartz-bearing pelitic rocks. *Contributions to Mineralogy and Petrology*, **20**, 244–267.

Cheng, H., Nakamura, E., Kobayashi, K. & Zhou, Z., 2007. Origin of atoll garnets in eclogites and implications for the redistribution of trace elements during slab exhumation in a continental subduction zone. *American Mineralogist*, **92**, 1119–1129.

Chernoff, C.B. & Carlson, W.D., 1999. Trace element zoning as a record of chemical disequilibrium during garnet growth. *Geology*, **27**, 555–558.

Clarke, G.L., Daczko, N.R. & Nockolds, C., 2001. A method for applying matrix corrections to X-ray intensity maps using the Bence-Albee algorithm and Matlab. *Journal of Metamorphic Geology*, **19**, 635–644.

Cunningham, W.D., 1993. Strike-slip faults in the southernmost Andes and the development of the Patagonian orocline. *Tectonics*, **12**, 169–186.

Cunningham, W.D., 1994. Uplifted ophiolitic rocks on Isla Gordon, southernmost Chile: implications for the closure history of the Rocas Verdes marginal basin and the tectonic evolution of the Beagle Channel region. *Journal of South American Earth Sciences*, **7**, 135–148.

Cunningham, W.D., 1995. Orogenesis at the southern tip of the Americas: the structural evolution of the Cordillera Darwin metamorphic complex, southernmost Chile. *Tectonophysics*, **244**, 197–229.

Dalziel, I.W.D., 1981. Back-arc extension in the southern Andes: a review and critical reappraisal. *Philosophical Transactions of the Royal Society of London Series A*, **300**, 319–335.

Dalziel, I.W.D. & Brown, R.L., 1989. Tectonic denudation of the Darwin metamorphic core complex in the Andes of Tierra del Fuego, southernmost Chile: implications for Cordilleran orogenesis. *Geology*, **17**, 699–703.

Dalziel, I.W.D. & Cortés, R., 1972. Tectonic style of the southernmost Andes and the Antarctandes. *XXIV International Geological Congress Section*, **3**, 316–327.

Dalziel, I.W.D. & Elliot, D.H., 1971. Evolution of the Scotia Arc. *Nature*, **233**, 246–252.

Dalziel, I.W.D., de Wit, M.J. & Palmer, K.F., 1974. Fossil marginal basin in the southern Andes. *Nature*, **250**, 291–294.

Darwin, C.R., 1846. *Geological Observations on South America. Being the Third Part of the Geology of the Voyage of the Beagle, Under the Command of Capt. Fitzroy, R.N. During the Years 1832 to 1836.* Smith Elder and Co., London, 279 pp.

Dott, R.H., Jr., Winn, R.D., de Wit, M.J. & Bruhn, R.L., 1977. Tectonic and sedimentary significance of Cretaceous Tekenika Beds of Tierra del Fuego. *Nature*, **266,** 620–622.

Dott, R.H., Winn, R.D. & Smith, C.H.L., 1982. Relationship of Late Mesozoic and Early Cenozoic sedimentation to the tectonic evolution of the southernmost Andes and Scotia Arc. In: *Antarctic Geoscience* (ed. Craddock, C.), pp. 193–201. University of Wisconsin Press, Madison.

Dubessy, J., Buschaert, S., Lamb, W., Pironon, J. & Thiéry, R., 2001. Methane-bearing aqueous fluid inclusions: Raman analysis, thermodynamic modelling and application to petroleum basins. *Chemical Geology*, **173,** 193–205.

Duncan, R.A., Hooper, P.R., Rehacek, J., Marsh, J.S. & Duncan, A.R., 1997. The timing and duration of the Karoo igneous event, southern Gondwana. *Journal of Geophysical Research*, **102,** 18127–18138.

Encarnación, J., Fleming, T.H., Elliot, D.H. & Eales, H.V., 1996. Synchronous emplacement of Ferrar and Karoo dolerites and the early breakup of Gondwana. *Geology*, **24,** 535–538.

Fan, H.-R., Xie, Y.-H., Wang, K.-Y. & Wilde, S.A., 2004. Methane-rich fluid inclusions in skarn near the giant REE-Nb-Fe deposit at Bayan Obo, Northern China. *Ore Geology Reviews*, **25,** 301–309.

Fildani, A. & Hessler, A.M., 2005. Stratigraphic record across a retroarc basin inversion: Rocas Verdes–Magallanes Basin, Patagonian Andes, Chile. *Geological Society of America Bulletin*, **117,** 1596–1614.

Fildani, A., Cope, T.D., Graham, S.A. & Wooden, J.L., 2003. Initiation of the Magallanes foreland basin: timing of the southernmost Patagonian Andes orogeny revised by detrital zircon provenance analysis. *Geology*, **31,** 1081–1084.

Foster, D.A. & Gray, D.R., 2000. Evolution and structure of the Lachlan Fold Belt (Orogen) of eastern Australia. *Annual Reviews in Earth and Planetary Sciences*, **28,** 47–80.

Fuenzalida, R. & Covacevich, C., 1988. Volcanismo y bioestratigrafía del Jurásico superior y Cretácico inferior en la cordillera Patagónica, región de Magallanes, Chile. *V Congreso Geológico Chileno, Tomo III*, H159–H183.

Ghiglione, M.C. & Ramos, V.A., 2005. Progression of deformation and sedimentation in the southernmost Andes. *Tectonophysics*, **405,** 25–46.

Gombosi, D.J., Barbeau, D.L. & Garver, J.I., 2009. New thermochronometric constraints on the rapid Paleogene exhumation of the Cordillera Darwin complex and related thrust sheets in the Fuegian Andes. *Terra Nova*, **21,** 507–515.

Grunow, A.M., Dalziel, I.W.D., Harrison, T.M. & Heizler, M.T., 1992. Structural geology and geochronology of subduction complexes along the margin of Gondwanaland: new data from the Antarctic Peninsula and southernmost Andes. *Geological Society of America Bulletin*, **104,** 1497–1514.

Gust, D.A., Biddle, K.T., Phelps, D.W. & Uliana, M.A., 1985. Associated Middle to Late Jurassic volcanism and extension in southern South America. *Tectonophysics*, **16,** 223–253.

Halpern, M., 1973. Regional geochronology of Chile south of 50° Latitude. *Geological Society of America Bulletin*, **84,** 2407–2422.

Halpern, M. & Rex, D.C., 1972. Time and folding of the Yahgan Formation and age of the Tekenika Beds, Southern Chile, South America. *Geological Society of America Bulletin*, **83,** 1881–1886.

Hames, W.E. & Menard, T., 1993. Fluid-assisted modification of garnet composition along rims, cracks, and mineral inclusion boundaries in samples of amphibolite facies schists. *American Mineralogist*, **78,** 338–344.

Hanson, R.E. & Wilson, T.J., 1991. Submarine rhyolitic volcanism in a Jurassic proto-marginal basin, southern Andes, Chile and Argentina. In: *Andean Magmatism and Its Tectonic Setting* (eds Harmon, R.S. & Rapela, C.), *Special Papers of the Geological Society of America*, **265,** 13–27.

Hanson, R.E. & Wilson, T.J., 1993. Large-scale rhyolite peperites (Jurassic, southern Chile). *Journal of Volcanology and Geothermal Research*, **54,** 247–264.

Harris, R., Kaiser, J., Hurford, A. & Carter, A., 2000. Thermal history of Australian Passive Margin cover sequences accreted to Timor during late Neogene arc-continent collision, Indonesia. *Journal of Asian Earth Sciences*, **18,** 47–69.

Hawkins, A.T., Selverstone, J., Brearley, A.J., Beane, R.J., Ketcham, R.A. & Carlson, W.D., 2007. Origin and mechanical significance of honeycomb garnet in high-pressure metasedimentary rocks from the Tauern Window, Eastern Alps. *Journal of Metamorphic Geology*, **25,** 565–583.

Hervé, F., Fuenzalida, J., Araya, E. & Solano, A., 1979. Edades radiometricas y tectonica Neogena en el sector costero de Chiloe Continental, Xa Region. *Congreso Geologico Chileno, 2nd, Arica, Chile, Acta*, **1,** F1–F18.

Hervé, F., Nelson, E., Kawashita, K. & Suárez, M., 1981. New isotopic ages and the timing of orogenic events in the Cordillera Darwin, southernmost Chilean Andes. *Earth and Planetary Science Letters*, **55,** 257–265.

Hervé, M., Suárez, M. & Puig, A., 1984. The Patagonian Batholith S of Tierra del Fuego, Chile: timing and tectonic implications. *Journal of the Geological Society, London*, **141,** 909–917.

Hervé, F., Pankhurst, R.J., Fanning, C.M., Calderón, M. & Yaxley, G.M., 2007. The South Patagonian batholith: 150 my of granite magmatism on a plate margin. *Lithos*, **97,** 373–394.

Hervé, F., Fanning, C.M., Pankhurst, R.J. et al., 2010. Detrital zircon SHRIMP U-Pb age study of the Cordillera Darwin Metamorphic Complex: sedimentary sources and implications for the evolution of the Pacific margin of Gondwana. *Journal of the Geological Society, London*, **8,** 555–568.

Holland, T.J.B. & Powell, R., 1990. An enlarged and updated internally consistent dataset with uncertainties and correlations: the system $K_2O-Na_2O-CaO-MgO-MnO-FeO-Fe_2O_3-Al_2O_3-TiO_2-SiO_2-C-H_2-O_2$. *Journal of Metamorphic Geology*, **8,** 89–124.

Hollister, L.S., 1966. Garnet zoning: an interpretation based on the Rayleigh fractionation model. *Science*, **154,** 1647–1651.

Katz, H.R., 1973. Contrasts in tectonic evolution of orogenic belts in the south-east Pacific. *Journal of the Royal Society of New Zealand*, **3,** 333–362.

Klepeis, K.A., 1994a. Relationship between uplift of the metamorphic core of the southernmost Andes and shortening in the Magallanes foreland fold and thrust belt, Tierra del Fuego, Chile. *Tectonics*, **13,** 882–904.

Klepeis, K.A., 1994b. The Magallanes and Deseado fault zones: major segments of the South American – Scotia transform plate boundary in southernmost South America, Tierra del Fuego. *Journal of Geophysical Research*, **99**(B11)**,** 22001–22014.

Klepeis, K.A. & Austin, J.A., 1997. Contrasting styles of superposed deformation in the southernmost Andes. *Tectonics*, **16,** 755–776.

Klepeis, K.A., Betka, P., Clarke, G.L. et al., 2010. Continental underthrusting and obduction during the Cretaceous closure of the Rocas Verdes rift basin, Cordillera Darwin, Patagonian Andes. *Tectonics*, **29,** TC3014, doi: 10.1029/2009TC002610.

Kohn, M.J., Spear, F.S. & Dalziel, I.W.D., 1993. Metamorphic P-T paths from Cordillera Darwin, a core complex in Tierra del Fuego, Chile. *Journal of Petrology*, **34,** 519–542.

Kohn, M.J., Spear, F.S., Harrison, T.M. & Dalziel, I.W.D., 1995. $^{40}Ar/^{39}Ar$ geochronology and P-T-t paths from the Cordillera Darwin metamorphic complex, Tierra del Fuego, Chile. *Journal of Metamorphic Geology*, **13,** 251–270.

Kraemer, P., 2003. Orogenic shortening and the origin of the Patagonian orocline (56° S Lat). *Journal of South American Earth Sciences*, **15,** 731–748.

Kranck, E., 1932. Geological investigations in the cordillera of Tierra del Fuego. *Acta Geograhpica Helsingfors*, **4**, 1–231.

Kretz, R., 1983. Symbols for rock-forming minerals. *American Mineralogist*, **68**, 277–279.

Lodolo, E., Menichetti, M., Bartole, R., Ben-Avraham, Z., Tassone, A. & Lippai, H., 2003. Magallanes-Fagnano continental transform fault (Tierra del Fuego, southernmost South America). *Tectonics*, **22**, 1076.

Loomis, T.P., 1975. Reaction zoning of garnet. *Contributions to Mineralogy & Petrology*, **52**, 285–305.

Ludwig, K.R., 2001. SQUID 1.02, A User's Manual. *Berkeley Geochronology Center Special Publication*, **No. 2**, Berkeley, CA, USA.

Ludwig, K.R., 2003. User's Manual for Isoplot/Ex, Version 3.0, A Geochronological Toolkit for Microsoft Excel. *Berkeley Geochronology Center Special Publication*, **No. 4**, Berkeley, CA, USA.

Marmo, B.A., Clarke, G.L. & Powell, R., 2002. Fractionation of bulk rock composition due to porphyroblast growth: effects on eclogite facies mineral equilibria, Pam Peninsula, New Caledonia. *Journal of Metamorphic Geology*, **20**, 151–165.

McAtamney, J., Klepeis, K., Mehrtens, C. & Thomson, S.N., 2009. The transition from extensional rift basin to compressional retro-arc foreland basin in the southernmost Andes (54.5°S): new provenance data from Bahía Brookes and Seno Otway. *Geological Society of America Abstracts with Programs*, **41**, 52.

Minor, D.R. & Mukasa, S.B., 1997. Zircon U-Pb and hornblende ^{40}Ar-^{39}Ar ages for the Dufek layered mafic intrusion, Antarctica: implications for the age of the Ferrar large igneous province. *Geochimica et Cosmochimica Acta*, **61**, 2497–2504.

Moore, T.K., 1990. *A Metamorphic and Kinematic Study of the Cordillera Darwin Metamorphic Core Complex, Southwestern Chile*. BSc thesis, Carleton University.

Mpodozis, C. & Allmendinger, R.W., 1993. Extensional tectonics, Cretaceous Andes, northern Chile (27°S). *Geological Society of America Bulletin*, **105**, 1462–1477.

Mukasa, S.B. & Dalziel, I.W.D., 1996. Southernmost Andes and South Georgia Island, North Scotia Ridge: zircon U-Pb and muscovite ^{40}Ar/^{39}Ar age constraints on tectonic evolution of Southwestern Gondwanaland. *Journal of South American Earth Sciences*, **9**, 349–365.

Natland, M.L., Gonzalez, E., Cañon, A. & Ernst, M., 1974. A system of stages for correlation of Magallanes basin sediments. *Memoirs of the Geological Society of America*, **139**, 126.

Nelson, E.P., 1982. Post-tectonic uplift of the Cordillera Darwin orogenic core complex: evidence from fission track geochronology and closing temperature-time relationships. *Journal of the Geological Society, London*, **139**, 755–761.

Nelson, E.P., Dalziel, I.W.D. & Milnes, A.G., 1980. Structural geology of the Cordillera Darwin – collisional-style orogenesis in the southernmost Chilean Andes. *Eclogae Geologicae Helvetiae*, **73**, 727–751.

Olivero, E.B. & Martinioni, D.R., 2001. A review of the geology of the Argentinian Fuegian Andes. *Journal of South American Earth Sciences*, **14**, 175–188.

Pankhurst, R.J., Riley, T.R., Fanning, C.M. & Kelley, S., 2000. Episodic silicic volcanism in Patagonia and the Antarctic Peninsula: chronology of magmatism associated with the break-up of Gondwana. *Journal of Petrology*, **41**, 605–625.

Pankhurst, R.J., Rapela, C.W., Loske, W.P., Marquez, M. & Fanning, C.M., 2003. Chronological study of the pre-Permian basement rocks of southern Patagonia. *Journal of South American Earth Sciences*, **16**, 27–44.

Powell, R. & Holland, T.J.B., 1988. An internally consistent thermodynamic dataset with uncertainties and correlations: 3. Application, methods, worked examples and a computer program. *Journal of Metamorphic Geology*, **6**, 173–204.

Powell, R., Holland, T.B.J. & Worley, B., 1998. Calculating phase diagrams involving solid solutions via non-linear equations, with examples using THERMOCALC. *Journal of Metamorphic Geology*, **16**, 577–588.

Spear, F.S. & Selverstone, J., 1983. Quantitative *P-T* paths from zoned minerals: theory and tectonic applications. *Contributions to Mineralogy and Petrology*, **83**, 348–357.

Stern, C.R., 1980. Geochemistry of Chilean ophiolites: evidence for the compositional evolution of the mantle source of back-arc basin basalts. *Journal of Geophysical Research*, **85**, 955–966.

Stern, C.R. & de Wit, M.J., 2003. Rocas Verdes ophiolites, southernmost South America: remnants of progressive stages of development on oceanic-type crust in a continental margin back-arc basin. In: *Ophiolites in Earth History* (eds Dilek, Y. & Robinson, P.T.). *Geological Society, London, Special Publications*, **218**, 1–19.

Stern, C.R., Mukasa, S.B. & Fuenzalida, P.R., 1992. Age and petrogenesis of the Sarmiento ophiolite complex of southern Chile. *Journal of South American Earth Sciences*, **6**, 97–104.

Stump, E., 1995. *The Ross Orogen of the Transantarctic Mountains*. Cambridge University Press, Cambridge, 284 pp.

Suárez, M. & Pettigrew, T.H., 1976. An Upper Mesozoic island-arc – back-arc system in the southern Andes and South Georgia. *Geological Magazine*, **113**, 305–328.

Suárez, M., Puig, A. & Hervé, M., 1985. Hoja Isla Hoste e islas adyacentes, XII Región, *Carta Geológica de Chile No. 65*, Servício Nacional de Geología y Minería de Chile, escala 1: 250.000, Santiago, 113 pp.

Tera, F. & Wasserburg, G.J., 1972. U-Th-Pb systematics in three Apollo 14 basalts and the problem of initial lead in lunar rocks. *Earth and Planetary Science Letters*, **14**, 281–304.

Wei, C., Wang, W., Clarke, G.L., Zhang, L. & Song, S., 2009. Metamorphism of high/ultrahigh-pressure pelitic-felsic schist in the South Tianshan Orogen, NW China: phase equilibria and P-T path. *Journal of Petrology*, **50**, 1973–1991.

White, R.W., Powell, R. & Holland, T.J.B., 2001. Calculation of partial melting equilibria in the system Na$_2$O-CaO-K$_2$O-FeO-MgO-Al$_2$O$_3$-SiO$_2$-H$_2$O (NCKFMASH). *Journal of Metamorphic Geology*, **19**, 139–153.

White, R.W., Powell, R. & Clarke, G.L., 2002. The interpretation of reaction textures in Fe-rich granulites of the Musgrave Block, central Australia: constraints from mineral equilibria calculation in the system K$_2$O-FeO-MgO-Al$_2$O$_3$-SiO$_2$-H$_2$O-TiO$_2$-Fe$_2$O$_3$. *Journal of Metamorphic Geology*, **20**, 41–55.

White, R.W., Powell, R. & Clarke, G.L., 2003. Prograde metamorphic assemblage evolution during partial melting of metasedimentary rocks at low pressures: migmatites from Mt Stafford, central Australia. *Journal of Petrology*, **44**, 1937–1960.

Whitney, D.L., 1991. Calcium depletion halos and Fe–Mn–Mg zoning around faceted plagioclase inclusions in garnet from a high-grade pelitic gneiss. *American Mineralogist*, **76**, 493–501.

Whitney, D.L., Mechum, T.A., Dilek, Y. & Kuehner, S.M., 1996a. Modification of garnet by fluid infiltration during regional metamorphism in garnet through sillimanite-zone rocks, Dutchess County, New York. *American Mineralogist*, **81**, 696–705.

Whitney, D.L., Mechum, T.A., Kuehner, S.M. & Dilek, Y.R., 1996b. Progressive metamorphism of pelitic rocks from protolith to granulite facies, Dutchess County, New York, USA: constraints on the timing of fluid infiltration during regional metamorphism. *Journal of Metamorphic Geology*, **14**, 163–181.

Williams, I.S., 1998. U-Th-Pb geochronology by ion-microprobe. In: *Applications of Microanalytical Techniques to Understanding Mineralizing Process* (eds McKibben, M., Shanks, W. & Ridley, W.) *Reviews in Economic Geology*, **7**, pp. 1–36. The Economic Geology Publishing Company, El Paso, TX.

Wilson, T.J., 1991. Transition from back-arc to foreland basin development in the southernmost Andes: stratigraphic record from the Ultima Esperanza District, Chile. *Geological Society of America Bulletin*, **103**, 98–111.

Winslow, M.A., 1982. The structural evolution of the Magallanes basin and neotectonics in the southernmost Andes. In:

Antarctic Geoscience (ed. Craddock, C.), pp. 143–154. University of Wisconsin Press, Madison.

de Wit, M., 1977. The evolution of the Scotia Arc as a key to the reconstruction of southwestern Gondwanaland. *Tectonophysics*, **37,** 53–81.

Worley, B. & Powell, R., 2000. High-precision relative thermobarometry; theory and a worked example. *Journal of Metamorphic Geology*, **18,** 91–101.

Wörner, G., Fricke, A. & Burke, E.A.J., 1993. Fluid-inclusion studies on lower crustal gabbroic xenoliths from the Mt. Melbourne Volcanic field (Antarctica): evidence for the post-crystallization uplift history during Cenozoic Ross Sea Rifting. *European Journal of Mineralogy*, **5,** 775–785.